Erasmus University Rotterdam

Erasmus School of Economics

Asymmetric volatility spillovers between cryptocurrency and financial markets: A time-varying VAR approach

Bachelor thesis BSc^2 Econometrics/Economics

Name student and student ID number: Nikita Pavlov (467307)

Supervisor: Martina D. Zaharieva, Second assessor: Terri van der Zwan

July 4, 2021

Abstract

This paper analyses asymmetric volatility spillovers between cryptocurrency and financial markets for the cryptos Bitcoin (*BTC*), Ethereum (*ETH*) and the financial markets Nikkei 225 (*N225*), Eurostoxx 50 (*STO50*) and S&P 500 (*SP500*) between 2017-2021, using a time-varying VAR approach. Evidence from orthogonalised impulse response functions (*IRFs*) shows that financial markets are immune to crypto shocks, such that financial market shocks unidirectionally transmit to crypto markets. The total volatility spillover index demonstrates that spillovers increase after major bear markets, representing greater market connectedness. Nevertheless, asymmetry in volatility spillovers is found through the spillover asymmetry measure (*SAM*), showing that positive spillovers dominate during stable bull markets, but negative spillovers surge quickly compared to positive spillovers during the COVID-19 crisis, originating from the financial markets. Moreover, forecast error variance decompositions (*FEVD*) surprisingly reveal that BTC innovations do not affect the forecast error variance of any markets, whereas ETH has a prominent negative volatility spillover to the financial markets, when crypto's mining difficulty was reduced at the end of 2018. Lastly, FEVDs also reveal that SP500 innovations explain the largest fractions of variance; though positive SP500 innovations explain a larger part than negative innovations.

Contents

1 Introduction

The cryptocurrency (from now on: "crypto") market has seen a stellar inflow of money in the past decade; with the most prominent crypto Bitcoin becoming the fastest asset to reach the $1 trillion market capitalisation. The over 4000 established cryptos are challenging the status-quo of traditional currencies, whereby cryptos are regulated through a decentralised system of computers with blockchain technology, rather than by central banks. More retailers are starting to accept cryptos as an alternative method of payment; with Tesla recently announcing that purchases can be made with Bitcoin (Katrina, 2021). But as Christine Lagarde once said, "markets love volatility", which is why currently cryptos are rather used as a speculative asset, due to its high volatility partly due to unregulated pump and dump schemes (Brauneis & Mestel, 2018). This high volatility has attracted many retail- and institutional investors with the hope of achieving high short-term returns when estimated correctly (French et al., 1987).

Given that cryptos are a recent phenomenon, research into volatility forecasting for this asset class has been scarce. With experts arguing that cryptos have no relationship with economic fundamentals, its growing popularity has raised questions as to whether cryptos are becoming more intertwined with other markets, such as financial markets. At the start of 2018, when Bitcoin's and Ethereum's bubble burst and its values dropped by an average of 40%, major financial indices also took a hit of an average of 9%. Liang & Baig (2021) finds that extreme Bitcoin price swings beyond +10% and -10% are more positively correlated with fluctuations in the financial markets than during normal trading situations and conclude that equity and crypto sentiments are becoming more connected. To further supplement this area of research with a more detailed analysis, the following research question is investigated:

Are asymmetric volatility spillovers present between cryptocurrency and financial markets and how does this vary over time?

Addressing above research question aids in establishing causal inferences for volatility forecasting in the crypto markets; as crypto's inter-linkage with financial markets has not been established yet. Thus, by also accounting the evidence of the leverage effect being present in equity (Bekaert & Wu, 2000) and crypto markets (Zhang et al., 2018), this research contributes towards understanding how upside- and downside volatility of financial markets impact crypto markets and vice versa. On the social relevance side, this analysis helps with reducing downside volatility and helps to better anticipate upside volatility, such that situations like the hedge fund Cryptolab Capital losing 100% of its assets under management can be prevented (Phillips, 2020). This research thus contributes towards (uninformed) investors seeking to improve portfolio diversification and risk evaluation strategies that are branching into the crypto markets.

This research addresses the spillovers with realised variances using high frequency intraday returns among two major cryptos, Bitcoin (*BTC*) and Ethereum (*ETH*) and three major financial markets, S&P 500 (*SP500*), Euro Stoxx 50 (*STO50*) and Nikkei 225 (*N225*) between 2017 and 2021. In addition, to assess the asymmetry of volatility spillovers, positive and negative semivariances are used, conditioned on positive and negative innovations in the returns of above markets (also known as good and bad volatilities). Such analysis is commonly performed using a vector autoregressive (VAR) model, but due to evidence of a large number of structural breaks in all markets, the time-varying parameter VAR (*TVP-VAR*) model is more suitable, where the variable ordering is determined using the directed acyclic graph (*DAG*) technique. From the estimated TVP-VAR coefficients and variance-covariance matrices, the volatility spillovers are determined using orthogonalised impulse response functions (*IRFs*) and forecast error variance decompositions (*FEVDs*) over several time horizons. The asymmetry of such spillovers is assessed with spillover asymmetry measures (*SAM*), the difference between the spillovers due to positive and negative semivariances. This is performed by looking at the total *SAM* and the contribution of individual markets to the asymmetry in the volatility transmission mechanism.

This analysis reveals that uni-directional exogenous shock transmissions from financial to crypto markets are present in the orthogonalised IRFs, as financial markets are immune to shocks in ETH and BTC. While the 1-day horizon FEVDs only show that BTC's variance is partially explained by ETH innovations, the 30-day horizon FEVDs display that SP500 innovations explain the largest part of the forecast error variances of all markets, though positive SP500 innovations have a larger impact than negative innovations. The most surprising result is that BTC innovations have little to no impact on other markets' variance, while negative ETH innovations explain a big part of all markets' variance at the end of 2018, due to the reduced crypto mining difficulty. Finally, the total volatility spillovers report that spillovers increase after bear markets, likely linked to the risk appetite being altered after a crisis, leading to investors homogenising market beliefs. In terms of volatility spillover asymmetry with *SAM*s, positive spillovers dominate negative spillovers during the stable bull market between the two bear markets, but due to the COVID-19 crisis, the overall negative spillovers quickly surge relative to positive spillovers.

The remainder of this paper contains the literature review in section 2, the methodology in section 3, the data section in 4, the results in section 5 and the conclusion & discussion in section 6.

2 Literature review

Forecasting volatility is a longstanding field of interest in the financial industry for risk evaluation, as equity- and crypto return data contain evidence for volatility clustering and leptokurtosis (Zhang et al., 2018). Models arose that deemed suitable to capture such properties in financial time series, such as generalised autoregressive conditional heteroskedasticity ($GARCH$) models, which can capture volatility persistence floating around the long-term mean (Bollerslev, 1986). As GARCH models assume symmetric distributions, further extensions have been proposed to improve forecasting performance, as evidence of the leverage effect was found in equity (Bekaert & Wu, 2000) and crypto markets (Zhang et al., 2018). This led to asymmetric modifications of the GARCH model, such as GJR-GARCH (Glosten et al., 1993) or Beta-t-EGARCH models (Harvey & Sucarrat, 2014), which have been shown to outperform the forecasting performance of the common volatility index VIX (Stein et al., 2020).

While above models are one-dimensional, Ross (1989) found that return volatility depends on the rate of information flow and that such information can be utilised for predicting volatility of other assets. Therefore, a N-dimensional adaptation of the univariate autoregressive models, the VAR model, is a better fit for analysing volatility spillovers. As the estimated parameters do not have a direct interpretation, VAR models are used in a moving average (MA) form, which enables VAR models to give economic interpretations through IRFs and FEVDs. IRFs and FEVDs track the effect of an exogenous shock in a specific variable at time t over a specific horizon. As such, VAR models are mainly used to analyse monetary policy effects on unemployment and inflation (C. A. Sims, 1980), but its application has been expanded to other financial variables, such as investigating the transmission mechanism among exchange rates of major currencies (Lee & Chinn, 1998), the transmission effects of Gross National Product (GNP) of several countries (Elwood, 1997) and (asymmetric) volatility spillovers between crude oil and financial markets (Wang & Wu, 2018).

To capture the dynamic transmission mechanism among variables in multivariate linear structures, C. Sims (1993) and Stock & Watson (1996) introduced a VAR model with drifting coefficients, though without time-varying residual variance-covariance matrices nor a dynamic simultaneous relationship among variables. Cogley & Sargent (2005) emphasised though that ignoring heteroskedasticity of innovations can estimate unreliable coefficients. Primiceri (2005) thus proposed a TVP-VAR model, that considered both time-varying coefficients and residual variance-covariance matrices, which would reflect the changing simultaneous relations among variables and heteroskedasticity (Primiceri, 2005). However, this model is an extreme case, as the coefficients and covariance matrices alter at every time period and thus assumes a structural break at every time period. Relaxations of this TVP-VAR model have been proposed in the form of a mixture innovation model, which only re-estimates the coefficients and covariance matrices at significant structural breaks (Koop et al., 2009). Nevertheless, we show that the high number of structural breaks for all markets still justifies the use of the TVP-VAR model of Primiceri (2005). Applications using TVP-VAR models also range from analysing monetary policy effects (Koop et al., 2009) to studying Gross National Product (GNP) of OECD countries (Chib & Greenberg, 1995), this time using a dynamic approach.

To use IRFs, it is assumed that the residual covariance matrix is diagonal. However, this usually does not hold in practice, as contemporaneous correlation among errors exists, implying that a shock in one variable may not be distinguishable from a shock in another variable, making IRFs biased (Swanson & Granger, 1997). This issue can be resolved through orthogonalised IRFs, using the Cholesky decomposition's lower triangular matrix. This ensures that all shocks become independent of each other, but also including the contemporaneous shock in other variables. However, its interpretability depends on the ordering of the variables, which assumes a subjective structural model of errors (Wang & Wu, 2018). To make the ordering of variables more data-driven, Swanson & Granger (1997) propose the DAG technique, to determine the ordering based on partial correlations and over-identifying restrictions on the contemporaneous shocks. Since Swanson & Granger (1997)'s methodology assumes a causal ordering with a recursive causation structure (meaning that each variable has only one cause), developments have been made which enable variables to have multiple causes, such as the PC algorithm by Spirtes et al. (2000).

(Asymmetric) volatility spillovers have been widely researched on several asset classes, such as credit risk spillovers among financial institutions (Yang & Zhou, 2013), spillovers between crude oil and financial markets (Wang & Wu, 2018) and in the forex market (Baruník et al., 2017). All papers found that asymmetry among good and bad volatility spillovers exists and that it changes over time due to events affecting the volatility spillovers, such as the financial crisis of 2008 in most of the findings. Furthermore, volatility spillovers have also been researched among cryptos (Wajdi et al., 2020), finding that spillovers among cryptos are bi-directional, but asymmetries in spillovers are dominated by bad rather than good volatilities. However, research is lacking in volatility spillovers between crypto markets and other asset classes, with only Malhotra & Gupta (2019) finding that uni-directional spillovers from Bitcoin to major Asian equity markets exist, while also showing that Bitcoin is a leading indicator of volatility for the remaining cryptos.

This paper fills the gap in research in asymmetric volatility spillovers between crypto- and financial markets on several details. Firstly, asymmetric volatility spillovers between cryptos and the major equity markets, such as the United States and Europe, have not been established yet. Secondly, Malhotra & Gupta (2019) only used squared daily returns in determining historical volatility, whereas realised variances and semivariances with intraday returns are better estimates of the true volatility (Andersen et al., 2001). Thirdly, this paper uses recent intraday return data between 2016 and 2021, a time period for which research has been sparse but contains important events, such as the Bitcoin and Ethereum crash at the start of 2018 and the COVID-19 crisis. Lastly, the models used in above research assume a constant mean over the full sample such that estimated coefficients are not time-varying, even though there is evidence of heteroskedasticity in both financial- and crypto markets (Gkillas & Katsiampa, 2018). Therefore, the TVP-VAR model by Primiceri (2005) is used to account for a dynamic volatility transmission mechanism.

3 Methodology

The code to execute the methods described below can be found in the accompanied *.zip* file, with a detailed description of all the scripts and functions to be found in Appendix A.

3.1 Realised variance, positive and negative semivariances

To analyse asymmetric volatility spillovers between crypto- and financial markets, realised variances, RV_t, are used as a proxy for the true daily volatility, as it gives a better indication of the reaction on price discovery while being an unbiased and consistent estimator of σ_t^2, the true daily variance (Andersen et al., 2001). At time t, the realised variance is calculated as follows, assuming that $r_{t,j}$ denotes the return of the jth interval of length 1/N during time t and that $r_{t,j}|I_{t-1} \sim i.i.d(0, \sigma_t^2/N)$:

$$RV_t = \sum_{j=1}^{N} r_{t,j}^2, t = 1, \ldots, T. \tag{1}$$

An asymmetric interpretation can be obtained from the realised variance through the positive and negative semivariances RS_t^+ and RS_t^-, such that $RV_t = RS_t^+ + RS_t^-$, where the variance is captured due to positive- and negative returns respectively (*i.e. good and bad volatilities*) and provides a good proxy for realised semivariances (Barndorff-Nielsen et al., 2008). RS_t^+ and RS_t^- are calculated as follows, where I(...) serves as an indicator function, as shown in (4):

$$RS_t^+ = \sum_{j=1}^{N} I(r_{t,j} \geq 0) r_{t,j}^2, \quad (2) \qquad RS_t^- = \sum_{j=1}^{N} I(r_{t,j} < 0) r_{t,j}^2. \quad (3) \qquad I(r_{t,j} \geq 0) = \begin{cases} 1, \text{if } r_{t,j} \geq 0 \\ 0, \text{otherwise} \end{cases} \quad (4)$$

3.2 VAR and its applications

To analyse volatility spillovers of multiple markets at the same time, a VAR model is used to obtain some of the specifications for the TVP-VAR model. As first introduced by C. A. Sims

(1980), a VAR(p) of lag order p is presented in (5), where RV_t and ϵ_t represent Nx1 vectors of endogenous variables (*i.e. the realised variances*) and white noise errors respectively for all t. The requirements for white noise errors are that $\mathrm{E}(\epsilon_t) = 0$, $\Sigma_\epsilon = \mathrm{E}(\epsilon_t \epsilon_t')$ is non-singular and ϵ_t and ϵ_v are independent when t≠v. A_i represents the NxN coefficient matrix for the ith lag order and the residual variance-covariance matrix $\Sigma_\epsilon = FDF'$, where F is a lower triangular with ones on the diagonal and D a diagonal matrix.

$$RV_t = \mu + \sum_{i=1}^{p} A_i RV_{t-i} + \epsilon_t \tag{5}$$

Even though IRFs, FEVDs and (asymmetric) volatility spillover indices are obtained with parameters from the TVP-VAR model, the VAR(p) model is used to obtain the optimal lag order p* for the TVP-VAR model. This is achieved using the Bayesian information criterium (BIC) and evaluating VAR(p) models with lag orders 1 to 15. Moreover, the residuals of the VAR(p*) model rather than the residuals of the TVP-VAR(p*) model are used to obtain a causal ordering of the markets with the DAG technique, due to reasons outlined in subsection 3.3.4.

3.3 TVP-VAR

3.3.1 TVP-VAR model description

Rather than employing the time-invariant VAR(p) model as introduced at (5), a TVP-VAR model is used, such that the coefficients and the residual variance-covariance matrices are dynamic, based on the relationship among the volatilities of the markets over time (Primiceri, 2005). The model is implemented in Matlab, using an adaptation of the code provided by Koop & Korobilis (2010). Assuming that the variances of all markets are stationary, the TVP-VAR(p) with lag order p is provided in (6), where RV_t and ϵ_t are Nx1 vectors of endogenous variables and white noise residuals respectively at time t, $A_{i,t}$ an NxN coefficient matrix of the ith lag order at time t and the residual variance-covariance matrix $\Sigma_{\epsilon,t} = F_t D_t F_t'$, where F_t is lower triangular with ones on the diagonal, D_t a diagonal matrix at time t. As can be seen, $A_{i,t}$, F_t and D_t are generalisations of the same variables in the VAR(p) model, such that they are time-varying.

$$RV_t = \mu_t + \sum_{i=1}^{p} A_{i,t} RV_{t-i} + \epsilon_t \tag{6}$$

To ensure that all markets are stationary for all variance types, the Augmented Dickey-Fuller (ADF) test is performed for every market in RV_t, RS_t^+ and RS_t^-, with H_0 that a unit root is present (thus non-stationary) and H_α that a unit root is not present. Also, as discussed in the literature review, the TVP-VAR(p) model of Primiceri (2005) assumes a changing coefficient and variance-covariance matrix at every time t, rather than a TVP-VAR(p) model that changes only at significant structural breaks (Koop et al., 2009). To show that all the variance types of all markets contain a high number of structural breaks that would justify the use of Primiceri's model, a Chow structural break test (see Chow (1960) for details on this test) at 5- and 10% significance levels is used to iteratively test with H_0 that a structural break is not present at every single time t and H_α otherwise.

As the coefficients of $A_{i,t}$, F_t and D_t are time-varying, the evolutions of $A_{i,t}$ and F_t are designed as a random walk model, as in (7) and (8) respectively, where $\alpha_t = vec(A_t')$ with $A_t = [A_{1,t}, \ldots, A_{p,t}]$ and ϕ_t is a $(\frac{N(N-1)}{2})$x1 vector of non-zero and non-one elements of the rows of F_t^{-1}. The standard deviations, where σ_t is a Nx1 vector of the diagonal elements of $D_t^{1/2}$, are modelled as a geometric random walk, as in (9). Moreover, all the innovations from (6)-(9); ϵ_t, ω_t, ψ_t and ξ_t follow a joint normal distribution with the corresponding variance-covariance matrix in (10), implying that all innovations are independent from each other. It is assumed that the variance-covariance matrix Ψ is block diagonal, with each block corresponding to parameters from separate equations, related to the different markets in RV_t. The reasoning behind this assumption becomes clear in the next section.

$$\alpha_t = \alpha_{t-1} + \omega_t \ , \omega_t \sim N(0, \Omega) \qquad (7) \qquad\qquad \phi_t = \phi_{t-1} + \psi_t \ , \psi_t \sim N(0, \Psi) \qquad (8)$$

$$\log \sigma_t = \log \sigma_{t-1} + \xi_t \ , \xi_t \sim N(0, \Xi) \qquad (9) \qquad V = Var\left(\begin{bmatrix} \epsilon_t \\ \omega_t \\ \psi_t \\ \xi_t \end{bmatrix}\right) = \begin{bmatrix} \Sigma_\epsilon & 0 & 0 & 0 \\ 0 & \Omega & 0 & 0 \\ 0 & 0 & \Psi & 0 \\ 0 & 0 & 0 & \Xi \end{bmatrix} \qquad (10)$$

3.3.2 Bayesian estimation of TVP-VAR parameters

For ease of understanding the concepts below, $x^T = [x_1', \ldots, x_T']'$ denotes a vector of variables x_t, which are time-varying, until a certain time period T.

The TVP-VAR(p) is a type of state space model, where the parameters α^T, ϕ^T, σ^T and the hyperparameters of matrix V are estimated using a Bayesian Markov Chain Monte Carlo (*MCMC*) simulation approach, the Gibbs sampler. A Bayesian approach is chosen rather than a maximum likelihood estimation (*MLE*) for a number of reasons. First, MLEs dealing with high dimensionality and nonlinearity have multiple peaks and may end up with estimated parameters far from the actual parameter space (Primiceri, 2005). Second, given that a TVP-VAR is a high-dimensional model, maximising MLE becomes a computationally demanding task. On the other hand, Bayesian methods handle high parameter dimensionality efficiently, as estimation problems are broken down into simpler ones.

The Gibbs sampler is a type of MCMC simulation method that can obtain any posterior distribution's statistic from N simulated draws, given that N is sufficiently large. However, this posterior distribution may be unknown and usually entails taking integrals, which may be intractable (Yildirim, 2012). The Gibbs sampler rather draws samples from the easier conditional posterior distributions of the parameters in question, holding all the other parameter values fixed. After an initial burn-in period, the draws converge to the joint posterior density. With a sufficient amount of draws, any point of the posterior density is guaranteed to be reached. Given the unobserved parameters $\alpha^T, \phi^T, \sigma^T$ and the hyperparameters of V (as given in (10), except Σ_ϵ as it can be derived from (6)), samples can be drawn from their conditional posterior distributions:

$$p(\alpha^T|RV^T, \phi^T, \sigma^T, V), \quad (11) \qquad p(\phi^T|RV^T, \alpha^T, \sigma^T, V), \quad (12) \qquad p(\sigma^T|RV^T, \alpha^T, \phi^T, V), \quad (13)$$

$$p(\Omega|RV^T, \alpha^T, \phi^T, \sigma^T), \quad (14) \qquad p(\Psi|RV^T, \alpha^T, \phi^T, \sigma^T), \quad (15) \qquad p(\Xi|RV^T, \alpha^T, \phi^T, \sigma^T). \quad (16)$$

For α^T, the density $p(\alpha^T|RV^T, \phi^T, \sigma^T, V) = p(\alpha_T|RV^T, \phi^T, \sigma^T, V)\prod_{t=1}^{T-1} p(\alpha_t|\alpha_{t+1}, RV^T, \phi^T, \sigma^T, V)$, where $\alpha_t|\alpha_{t+1}, RV^T, \phi^T, \sigma^T, V \sim N(B_{t|t+1}, P_{t|t+1})$, such that $B_{t|t+1}$ and $P_{t|t+1}$ represent the mean and the variance, respectively. As follows, the α^T vector can be easily drawn for all time periods t from this conditional distribution, as $B_{t|t+1}$ and $P_{t|t+1}$ can be derived by forward recursion (also known as the Kalman filter, see Carter & Kohn (1994) for more details) and backward recursion, given the models in (6) and (7). Furthermore, the hyperparameters of the model, being the diagonal blocks of V: Ω, Ξ and the diagonal blocks of Ψ, all follow an independent inverse-Wishart posterior distribution, as will be shown in section 3.3.3. Conditioned on the other fixed parameters as in (14)-(16), drawing samples from this distribution is easy as all innovations are observable.

Due to issues outlined in Appendix B, drawing samples of ϕ^T is not as easy as with α^T and requires the additional assumption of Ψ being block diagonal, such that the Kalman filter and backward recursion can be used equation by equation. The recursive procedure can then recover $\mu_{i,t|t+1} = E(\phi_{i,t}|\phi_{i,t|t+1}, RV^t, \alpha^T, \sigma^T, V)$ and $\nu_{i,t|t+1} = Var(\phi_{i,t}|\phi_{i,t|t+1}, RV^t, \alpha^T, \sigma^T, V)$ for the ith equation, which would give $p(\phi_{i,t}|\phi_{i,t+1}, RV^t, \alpha^T, \sigma^T, V) \sim N(\mu_{i,t|t+1}, \nu_{i,t|t+1})$. Then as with α^T, it is easy to draw samples from this Gaussian distribution. Furthermore, drawing samples of σ^T involves a more elaborate methodology, which can be found in Primiceri (2005).

After all the simulation draws, the burn-in draws will be discarded and the remaining draws are used to calculate the posterior means, which are essentially the estimated parameters and hyperparameters, for all time periods. To summarise, all the parameters are obtained using the Gibbs sampler's pseudo-code, as outlined below.

3.3.3 Initialising priors

As shown in the pseudo-code, all the parameters have to be initialised, such that the Gibbs sampler can be guaranteed to converge to the true joint posterior density during the burn-in

Algorithm 1 The Gibbs sampler for obtaining draws of the (hyper)parameters

```
Initialise $\phi^T, \sigma^T, s^T, V$;
for $i := 1$ to (burn-in draws + draws) do
    Draw $\alpha^T$ from $p(\alpha^T|RV^T, \phi^T, \sigma^T, V)$;
    Draw $\phi^T$ from $p(\phi^T|RV^T, \alpha^T, \sigma^T, V)$;
    Draw $\sigma^T$ from $p(\sigma^T|RV^T, \alpha^T, \phi^T, V)$;
    Draw V, by drawing $\Omega$, $\Psi$ and $\Xi$ from $p(\Omega, \Psi, \Xi|RV^T, \alpha^T, \phi^T, \sigma^T) = p(\Omega|RV^T, \alpha^T, \phi^T, \sigma^T) * p(\Xi|RV^T, \alpha^T, \phi^T, \sigma^T) * p(\Psi_1|RV^T, \alpha^T, \phi^T, \sigma^T) * \ldots * p(\Psi_{n-1}|RV^T, \alpha^T, \phi^T, \sigma^T)$;
    if $i >$ burn-in draws then
        Store $\alpha^T, \phi^T, \sigma^T$ and $V$ draws;
End for
Obtain the average of the $\alpha^T, \phi^T, \sigma^T$ and $V$ draws, representing the posterior mean;
```

draws. The approach of Primiceri (2005) is used to calibrate the prior distributions as seen in (17)-(22), using the first 20% of observations of RV_t, RS_t^+ and RS_t^-, denoted by τ. This initial subsample is used to derive coefficient estimates of a standard VAR(p*) (as in (5)), $\hat{\alpha}_{OLS}$, which is fed into the Gaussian distribution of α_0. The same method is used to estimate $\hat{\phi}_{OLS}$, that feeds into the Gaussian distribution of ϕ_0. For log σ_0, the mean of the Gaussian distribution is set to the log of the point estimate of the standard errors of the normal VAR(p*) and the identity matrix is to be arbitrarily chosen as the variance. As mentioned before, all hyperparameters of V follow an inverse-Wishart prior distribution. The inverse-Wishart distributions use $k_\Omega = 0.01$, $k_\Psi = 0.1$ and $k_\Xi = 0.01$, as recommended by Primiceri (2005), though he also found that results are rather robust to different ks. Do note that the ks do not influence the time variation, but rather the prior beliefs about the magnitude of time variation.

$$\alpha_0 \sim N(\hat{\alpha}_{OLS}, 4 * V(\hat{\alpha}_{OLS})) \quad (17) \qquad \phi_0 \sim N(\hat{\phi}_{OLS}, 4 * V(\hat{\phi}_{OLS})) \quad (18) \qquad \log \sigma_0 \sim N(\log \hat{\sigma}_{OLS}, I_N) \quad (19)$$

$$\Omega \sim IW(k_\Omega^2 * \tau * V(\hat{\alpha}_{OLS}), \tau) \quad (20) \qquad \Xi \sim IW(k_\Xi^2 * I_N, 2) \quad (21) \qquad \Psi \sim IW(k_\Psi^2 * V(\hat{\phi}_{OLS}), 2) \quad (22)$$

3.3.4 Ordering of variables: Directed acyclic graph technique

As introduced, the ordering of the variables of a VAR is important for the Cholesky decomposition, as with different orderings, the conclusions of IRFs and FEVDs are altered, in case contemporaneous correlation among errors exists. Therefore, the DAG technique is employed to obtain a data-driven ordering of the variables. However, Primiceri (2005) stated that the ordering of the variables for a TVP-VAR(p) model only slightly altered the analysis. Nevertheless, this paper aims for a more credible ordering of markets rather than a random ordering, based on a combination of subjective and data-driven reasoning, which would ease the interpretation of the results.

The DAG technique makes use of partial correlations and over-identifying restrictions on contemporaneous shocks. As the DAG technique cannot be directly applied to a TVP-VAR model, this paper uses the residuals of the VAR(p*) process to obtain a causal ordering for

RV_t, RS_t^+ and RS_t^-, together with economic reasoning. While the details of the DAG technique can be found in Hoover (2005), the PC algorithm is used, developed by Spirtes et al. (2000) and the Python code provided by Kalisch & Bühlman (2007), to obtain the causal ordering among the residuals of the VAR(p*) process over the full sample.

The PC algorithm assumes at first that all markets are linked with each other with an undirected link, from which two main stages take place: elimination and orientation. First, the elimination stage removes the links between markets that are not unconditionally correlated, which are markets that have no direct (directional) link with each other. Contrarily, conditional correlation implies that two markets are indirectly correlated with each other, if these two markets have both a causal link with another market. Then, the partial correlations between two markets, conditioned on a third market, are used to eliminate links between any market pair that is unconditionally uncorrelated. It then further tests for absence of conditional correlation among market pairs, then on sets of three or more markets. With this information, links are eliminated when no conditional correlation is present. Lastly, in the orientation stage, every conditionally uncorrelated market pairs and pairs causally connected along undirected paths through a third market are considered, whether improvements of the paths can be made. Thus, using this method, a DAG can be obtained, based on significant correlations among the markets. As this is a standard procedure in previous research (Hoover, 2005), the correlations are tested whether they are significantly different from zero at a 1% significance level.

3.4 Orthogonalised impulse response functions

To improve the interpretability of the TVP-VAR model, orthogonalised IRFs are used, as implemented by Lütkepohl (2005). IRFs describe the response of a variable to an exogenous shock in one variable at time t, which is otherwise not directly observed through the noisy coefficient estimates. Before introducing this application, it is important to rewrite the TVP-VAR(p) as a TVP-VAR(1) process as in (23), where $\boldsymbol{RV_t}$ and $\boldsymbol{e_t}$ are Npx1 vectors of the endogenous variables from the last p lagged observations and the residuals respectively at time t (Notice that these vectors are different from the vectors of a TVP-VAR(p) process) and $\boldsymbol{A_t}$ is a NpxNp matrix, which contains the coefficient matrices of the TVP-VAR(p) model in the first N rows. Please refer to Appendix B as to why these forms of the TVP-VAR model are equivalent.

$$\boldsymbol{RV_t} = \boldsymbol{A_t}\boldsymbol{RV_{t-1}} + \boldsymbol{e_t}, \text{where } \boldsymbol{RV_t} = \begin{pmatrix} RV_t \\ \vdots \\ RV_{t-p+1} \end{pmatrix}, \boldsymbol{e_t} = \begin{pmatrix} \epsilon_t \\ 0 \\ \vdots \\ 0 \end{pmatrix}, \boldsymbol{A_t} = \begin{pmatrix} A_{1,t} & \dots & A_{p-1,t} & A_{p,t} \\ I_N & \dots & 0 & 0 \\ \vdots & \ddots & \vdots & \vdots \\ 0 & \dots & I_N & 0 \end{pmatrix} \tag{23}$$

This TVP-VAR(1) representation can be converted into an MA representation as in (24), where the orthogonalised coefficient matrix $\Theta_{i,t} = \Phi_{i,t} P_t$ and the orthogonalised residuals vector $w_t = P_t^{-1}\epsilon_t$, with $\Phi_{i,t} = J\boldsymbol{A}_t^i J'$, where J = $[I_N : 0 : \ldots : 0]$ is a NxNp matrix and $\boldsymbol{A}_t$ is the coefficient matrix from the TVP-VAR(1) model from (23). P_t is a lower triangular matrix coming from the Cholesky decomposition of the residual variance-covariance matrix $\Sigma_{\epsilon,t} = P_t P_t'$ and ϵ_t being the residual vector from the TVP-VAR(p) process.

$$RV_t = \sum_{i=0}^{\infty} \Phi_{i,t} P_t P_t^{-1} \epsilon_{t-i} = \sum_{i=0}^{\infty} \Theta_{i,t} w_{t-i}. \tag{24}$$

This MA representation enables us to track an exogenous shock's effect throughout time. Through orthogonalisation, which is achieved by post- and pre-multiplying $\Phi_{i,t}$ and ϵ_t with P_t and P_t^{-1} respectively, it is ensured that a shock in one variable is uncorrelated and thus independent from a shock in another variable in contemporaneous time. While the details are left for Appendix B, this means that the orthogonalised IRF, at time t, can be traced over a certain time horizon H as follows, where the kth column of $\Theta_{i,t}$ corresponds to the response of all markets to an exogenous shock of the kth market:

$$\Theta_{0,t} = P_t \quad , \quad \Theta_{1,t} = \Phi_{1,t} P_t \quad , \quad \ldots \quad , \quad \Theta_{H,t} = \Phi_{H,t} P_t. \tag{25}$$

Thus, the initial shock at time t is the Cholesky decomposition's lower triangular matrix P_t, propelled over the H time observations with $\Phi_{i,t}$. Notice though that $\Phi_{i,t}$ from (24) could be calculated using $\boldsymbol{A}_t$ from the time periods t, t+1, ... , t+H, with the extra given information at each time period. However, this approach is not used as it would be computationally demanding. Nevertheless, due to P_t varying over time, the orthogonalised IRFs are still time-varying, adjusting to the changing dynamics among the volatility spillovers across the markets.

While the rest of the methods focus on the asymmetry among good and bad volatilities, the orthogonalised IRFs are only used with RV_t, such that the effect of exogenous shocks among the realised variances of the markets can be explored. Given that such an analysis is time-varying, orthogonalised IRFs are only performed at time periods when the highest realised variance is noted for the market in which the exogenous shock occurs. This effect is illustrated over a time horizon of 21 days. Moreover, the orthogonalised IRFs are scaled, by dividing it by the variance of the corresponding market extracted from $\Sigma_{\epsilon,t}$, such that the IRFs of all markets can be shown together. This gives insight as to how all the markets absorb an exogenous shock, more specifically a higher than usual exogenous shock in a particular market and how this differs across shocks from different markets. Since $\boldsymbol{A}_t$ and P_t can be generated at every draw in the Gibbs sampler, orthogonalised IRFs are performed at every draw of the simulation, from which the average impulse response is obtained. To account for the uncertainty of impulse responses, the IRFs of all markets are displayed with the 16th and 84th quantiles of the impulse response draws in Appendix D, such that these are the results ±1 standard deviation away from the mean of the Gaussian distribution.

3.5 Forecast error variance decompositions

IRFs only focus on the response of an exogenous shock. On the other hand, FEVDs focus on the fraction of variance of a certain variable that is explained by a shock in another variable. Furthermore, by looking at different time horizons, the evolution of this explanatory power in explaining variance can be observed. This would give insightful information as to how long and to what extent volatilities of crypto markets impact volatilities in the financial markets, and vice versa. As with IRFs, FEVDs also vary over time due to the dynamic coefficient matrix $\boldsymbol{A}_t$ and Cholesky decomposition's lower triangular matrix P_t. As with IRFs, the FEVDs are also implemented using the method of Lütkepohl (2005).

$$FE_{t,H} = \sum_{h=0}^{H-1} \Theta_{i,t} w_{t+H-h} \tag{26}$$

$$MSE_{j,t,H} = \sum_{n=1}^{N} (\theta^2_{jn,0,t} + \ldots + \theta^2_{jn,h-1,t}) = \sum_{i=0}^{H-1} \sum_{n=1}^{N} \theta^2_{jn,i,t} \tag{27}$$

By still using the orthogonalised MA representation of the TVP-VAR(p) process in (24), the optimal forecast error for a certain time horizons H is presented in (26), with $\Theta_{i,t}$ and w_t still defined exactly the same. $\Theta_{i,t}$ is built up of $\theta_{mn,i,t}$, representing the mn-th element of this matrix, where the jth row represents the forecast error for the jth market. Intuitively, this means that the jth row's forecast error is composed of the orthogonalised residuals of all the markets, $w_{1t}, \ldots, w_{Nt}$ and thus the forecast error consists of a combination of these orthogonalised shocks. Do note that this does not mean that every market's shock affects another market's forecast error, as $\theta_{mn,i,t}$ may be zero. For the FEVD, the jth varaible's Mean Squared Error (MSE) is required, as derived in (27).

$$FEVD_{jk,t,H} = \frac{\sum_{i=0}^{H-1} (e'_j \Theta_{i,t} e_k)^2}{MSE_{j,t,H}} \tag{28}$$

The contribution of the kth market's innovation to the forecast error variance of the jth market for a certain forecasting horizon H, represented by $FEVD_{jk,t,H}$, can be obtained as in (28). The multiplication $(e'_j \Theta_i e_k)^2$, where e_j is the jth column of the identity matrix I_N, retrieves the kth market's innovation effect on the jth market's variance. By dividing it by the $MSE_{j,t,H}$, the $FEVD_{jk,t,H}$ can be obtained. As previously explained, the $FEVD_{jk,t,H}$ changes over time, due to the time-varying coefficient matrix. Therefore, the $FEVD_{jk,t,H}$ is recorded for all time t for every market, with the hope that significant events in the crypto- and/or financial markets can be seen to significantly affect FEVDs. Moreover, the asymmetry between the effect of positive and negative innovations on the forecast error variance is analysed, by comparing FEVDs with RS^+_t and RS^-_t. As with IRFs, FEVDs can be also recorded at every Gibbs

Sampler's draw, from which the empirical mean is obtained for visualisation purposes. Lastly, FEVDs are performed with forecasting horizons of 1, 10 and 30 days, such that a decomposition can be obtained in the short-term, medium-term and long-term.

3.6 Asymmetric volatility spillovers indices

Besides IRFs and FEVDs, the linkages between the cryptos and financial markets in terms of volatility can be further explained by volatility spillovers indices. For better understanding, the non-orthogonalised MA form of a TVP-VAR(p) process is used, as in (29), where it still holds that $\Phi_{i,t} = J\boldsymbol{A}_t^i J'$.

$$RV_t = \sum_{i=0}^{\infty} \Phi_{i,t}\epsilon_{t-i} \tag{29}$$

Following Diebold & Yılmaz (2014) and Wang & Wu (2018), the directional volatility spillover from market j to i, $S^H_{i\leftarrow j,t}$, is determined by (30), where $\phi_{h,ij,t}$ is the ijth element of the $\Phi_{h,t}$ matrix that tracks the H-step-ahead forecast error variance of market i due to shocks in market j at time t, whereas the denominator accounts for the total H-step-ahead forecast error variation. It is an approximate measure of the volatility spillovers' intensity between those two markets. Notice that $\phi^2_{h,ij,t}$ could be replaced by $\phi^2_{h,ij,t+H-h}$ in (30), but this would imply using out-of-sample information which is undesirable, given that we are determining the forecast error. And as with impulse responses, using $\phi^2_{h,ij,t+H-h}$ would also be computationally demanding, thus substantiating enough reasoning for using $\phi^2_{h,ij,t}$ only at time t. Also note that $S^H_{i\leftarrow j,t}$ and $S^H_{j\leftarrow i,t}$ could differ from each other, due to bilateral imports and exports differences (Wang & Wu, 2018). But as can be seen, this volatility spillover uses FEVDs to give further interpretation to the TVP-VAR(p) model.

$$S^H_{i\leftarrow j,t} = \frac{\sum_{h=0}^{H-1} \phi^2_{h,ij,t}}{\sum_{h=0}^{H-1} trace(\Phi_{h,t}\Phi'_{h,t})} \tag{30}$$

$$S^H_t = \frac{1}{N}\sum_{i,j=1 i\neq j}^{N} S^H_{i\leftarrow j,t} = \frac{1}{N}\frac{\sum_{i,j=1 i\neq j}^{N}\sum_{h=0}^{H-1} \phi^2_{h,ij,t}}{\sum_{h=0}^{H-1} trace(\Phi_{h,t}\Phi'_{h,t})} \tag{31}$$

(30) is a stepping stone for the total directional spillover index in (31), by summing over all the non-diagonal elements of $\Phi_{h,t}$ for every h within the time horizon H. This index quantifies all the markets' spillover of volatility shocks and determines its contribution to the total forecast error variance. This method complements Diebold & Yılmaz (2014) and Wang & Wu (2018), through having a time-varying coefficient rather than a rolling or expanding window Φ_h, which further helps with capturing the volatility dynamics among the crypto- and financial markets.

The above volatility spillover indices can be extended to examine asymmetries among good and bad volatilities. Rather than using RV_t as the endogenous variable vector in the TVP-VAR(p) model, it can be replaced by the positive semivariance RS_t^+ and the negative semivariance RS_t^- vectors. By using the estimated coefficients from the models with these endogenous variables, the total spillover indices for the semivariances can be obtained using (31), represented by $S_t^{+,H}$ and $S_t^{-,H}$, which can also be referred to as positive and negative spillovers, respectively. From Baruník et al. (2016), the total spillover asymmetry measure (SAM) as in (32) is used to quantify the positive and negative spillovers' difference. These SAMs can be interpreted in multiple ways: it displays whether positive or negative spillovers dominate, thus serving as an estimate of the positive and negative market expectations at any given time, while it can also indicate how investors react to good and bad news and thus provide a sign of optimism or pessimism of the overall financial landscape. When $SAM_t^H > 0$, it implies that spillovers from RS_t^+ are larger than the spillovers from RS_t^-, with $SAM_t^H < 0$ otherwise.

$$SAM_t^H = S_t^{+,H} - S_t^{-,H} \tag{32}$$

$$SAM^H_{i\rightarrow\bullet,t} = S^{+,H}_{i\rightarrow\bullet,t} - S^{-,H}_{i\rightarrow\bullet,t} \tag{33}$$

$$SAM^H_{i\leftarrow\bullet,t} = S^{+,H}_{i\leftarrow\bullet,t} - S^{-,H}_{i\leftarrow\bullet,t} \tag{34}$$

This total SAM can be also be decomposed into identifying asymmetric volatility spillovers from a specific market i to all other markets, as in (33). $S^{+,H}_{i\rightarrow\bullet}$ and $S^{-,H}_{i\rightarrow\bullet}$ are derived from (31), where the summation $\sum_{i,j=1 i\neq j}^{N}$ in the nominator is replaced by $\sum_{j=1,j\neq i}^{N}$, such that the nominator becomes the sum of all the elements of just the ith row of $\Phi_{h,t}$ for $i \neq j$. A similar asymmetric spillover identification can be calculated going from all other markets to market j, as in (34). $S^{+,H}_{i\leftarrow\bullet}$ and $S^{-,H}_{i\leftarrow\bullet}$ are derived from (31), but this time the $\sum_{i,j=1 i\neq j}^{N}$ in the nominator is rather replaced by $\sum_{i=1,j\neq i}^{N}$, such that the nominator becomes the sum of all the elements of just the jth column of $\Phi_{h,t}$ for $i \neq j$. This approach complements the approach of Baruník et al. (2016), as rather than using a rolling window Φ_i, this paper uses $\Phi_{i,t}$ that is derived from the posterior mean of $\boldsymbol{A}_t$ from the Gibbs Sampler, therefore bypassing directly the rolling or expanding window approach.

4 Data

The research is performed on two cryptocurrencies and three stock indices. The cryptos Bitcoin (BTC) and Ethereum (ETH), expressed in USD, are used as these currently are the two most valuable cryptos, while BTC and ETH are also known to propel other smaller cryptos. For the financial markets, the S&P 500 (*SP500*), Eurostoxx 50 ($STO50$) and Nikkei 225 (*N225*) indices are used, as these are representable of the state of financial markets in the United States, Europe and Asia, respectively. All indices are based on the weighted free-float market capitalization of the underlying assets and are highly liquid. Do note that the crypto and financial markets differ, in the sense that crypto markets are open for trade 24/7, whereas financial markets are open for trade only on weekdays for a limited time. Therefore, only the days on which data from all markets is available are used.

Due to ETH only existing from late 2015, overlapping closing prices of the above-mentioned markets are obtained at a 30-minute frequency between 10th May 2016 and 30th April 2021, giving a total of 1551 observations for RV_t, RS_t^+ and RS_t^-. Higher frequency intraday data, such as 5-minute intervals, were not found, though Wang & Wu (2018) found that the *SAM* indices were robust to lower frequency data. BTC and ETH closing prices are retrieved from Crypto Data Download from the Gemini exchange, while closing prices for the stock indices are extracted from Bloomberg.

As described in section 3.3.3, the first 20% of observations are used to calibrate the prior conditional distributions, thus the first 230 observations (2016/05/10-2017/04/25) are used. Therefore, all the IRFs, FEVDs and volatility spillover indices are covered between 2017/04/26 and 2021/04/30. Even though the dataset only contains four years, it still contains two major bear markets, partly resembled by the heightened volatility observed in those time periods: December 2017- February 2018, related to the first time the crypto market's bubble burst, where ETH and BTC saw returns of -38.95% and -58.26% respectively and the financial markets taking an average hit of -9%. The second bear market is the COVID-19 crisis during February 2020-March 2020, when the financial markets narrowed by an average of 31% and ETH and BTC lost 50% and 37% of its value, respectively. What then followed, was a remarkable recovery of the markets. Other interesting events occured, such as ETH hitting its all time high on 2018/10/01 due to the Cryptokitties craze and BTC also hitting all time highs in April 2021, due to Tesla accepting Bitcoin as a method of payment.

Table 1: Descriptive statistics for RV_t , RS_t^+ and RS_t^-

	Mean	Std.dev.	Skew	Kurt	Min	Max
$\boldsymbol{RV_t}$						
ETH	0.00523	0.01615	17.00442	411.31533	0.00000	0.42714
BTC	0.00235	0.00853	19.87679	515.99921	0.00000	0.23790
N225	0.00014	0.00034	9.56917	142.00363	0.00000	0.00678
STO50	0.00015	0.00054	12.97151	208.59638	0.00000	0.01032
SP500	0.00012	0.00051	15.05690	304.05599	0.00000	0.01231
$\boldsymbol{RS_t^+}$						
ETH	0.00241	0.00513	6.27413	57.63413	0.00000	0.07668
BTC	0.00101	0.00244	10.01749	157.98359	0.00000	0.04986
N225	0.00007	0.00019	9.18936	111.56571	0.00000	0.00285
STO50	0.00007	0.00017	7.44491	64.48720	0.00000	0.00202
SP500	0.00006	0.00006	11.41223	165.84608	0.00000	0.00379
$\boldsymbol{RS_t^-}$						
ETH	0.00282	0.00282	25.51270	763.81900	0.00000	0.42637
BTC	0.00134	0.00133	26.60013	808.32271	0.00000	0.23763
N225	0.00007	0.00025	11.90041	212.82508	0.00000	0.00546
STO50	0.00008	0.00045	16.14352	300.94403	0.00000	0.00980
SP500	0.00007	0.00041	20.87345	528.93258	0.00000	0.01139

Table 1 presents the descriptive statistics for every market for RV_t, RS_t^+ and RS_t^-. ETH enjoys the highest mean volatility across all variance types, reaching a max of 0.00523 with RV_t, but it should also be noted that the mean and standard deviations of both cryptos are proportionately much higher than the volatilities of the financial markets, with the mean ranging between 0.00101 and 0.00523 for both cryptos across all variance types, whereas for N225, STO50 and SP500 ranges between 0.00006 and 0.00015. This exemplifies the high volatility that crypto markets have compared to financial markets. Comparing RS_t^+ with RS_t^-, the mean volatility is higher for RS_t^- for all markets except for N225, where the RS_t^+ and RS_t^- mean volatilities are the same. This thus illustrates the leverage effect that is found in both crypto- and financial markets, whereby investors are more concerned about downside- rather than upside risk. Lastly, all markets under all variance types exhibit skewnesses significantly different 0, while all kurtoses range between 57.634 and 808.322. This strongly indicates that the variances of all markets do not follow a normal distribution, and are heavy tailed.

Table 2: The correlation matrix for RV_t

Markets	ETH	BTC	N225	STO50	SP500
ETH	1.000				
BTC	0.849	1.000			
N225	0.151	0.206	1.000		
STO50	0.101	0.157	0.532	1.000	
SP500	0.110	0.188	0.495	0.779	1.000

Besides the descriptive statistics, Table 2 contains the correlations among the market for RV_t, with the correlations for RS_t^+ and RS_t^- presented in Table C.1 in the Appendix. It can be clearly seen that ETH and BTC are highly correlated with each other, with a value of 0.849. Meanwhile, both cryptos are less correlated with the stock indices, but still significantly different from 0, ranging between 0.101 and 0.151 for ETH and 0.157 and 0.206 for BTC with the N225, STO50 and SP500 markets. Among the financial markets, the highest correlation is observed between STO50 and SP500, while the correlation is around 0.5 for both markets with N225. This already gives a clue that the volatility transmission mechanism is likely to not be high between the crypto- markets and financial markets, but it does display that within the crypto and financial markets, higher volatility spillovers are likely to be seen.

5 Results

5.1 Checking assumptions of TVP-VAR(p)

As stated in the methodology, the number of structural breaks, the optimal lag order and whether or not all markets are stationary under all variance types are examined for the TVP-VAR(p) model. Firstly, Table 3 shows that most markets under all variance types have a high number of significant structural breaks, according to the Chow test, with BTC, N225, STO50 and SP500

Table 3: The number of significant structural breaks per market, for 5- and 10% significance levels.

Significance level	**0.05**			**0.1**		
	RV_t	RS_t^+	RS_t^-	RV_t	RS_t^+	RS_t^-
ETH	164	1061	21	192	1068	36
BTC	476	653	116	564	708	276
N225	764	696	434	860	878	566
STO50	1069	1098	960	1085	1104	1024
SP500	454	451	374	492	493	415

having on average a structural break every 1 to 3 days (over a total of 1551 observations). ETH is the anomaly among the markets, by only having 164 and 21 significant structural breaks for RV_t and RS_t^- respectively, though having 1061 significant breaks for RS_t^+ at the 5% significance level. For BTC, the number of significant breaks for RS_t^- is much lower than for RV_t and RS_t^+. Nevertheless, the majority of the markets show that a lot of significant structural breaks are present in the dataset, likely due to the high number of volatility outliers as seen in Table 1. This provides evidence that a TVP-VAR(p) with time-varying parameters at every time period is reasonable to be adopted for this paper's purposes.

Table 4: Test-statistics for the augmented Dickey-Fuller test for stationarity

	ETH	**BTC**	**N225**	**STO50**	**SP500**
$\boldsymbol{RV_t}$	-14.340***	-20.329***	-5.840***	-7.226***	-6.257***
$\boldsymbol{RS_t^+}$	-6.389***	-5.753***	-6.949***	-5.869***	-4.889***
$\boldsymbol{RS_t^-}$	-32.302***	-22.097***	-5.980***	-6.758***	-5.860***

Note. * $= p < 0.1$, ** $= p < 0.05$, *** $= p < 0.01$.

In terms of the TVP-VAR(p*) process itself, according to the BIC, the optimal lag orders for a time-invariant VAR(p*) process are 5, 3 and 5 for RV_t, RS_t^+ and RS_t^-, respectively. However, Primiceri (2005) stated that parameters would be ill-determined, if the number of estimated parameters is high for the limited number of iterations to be run with the Gibbs Sampler. To reduce the chance of ill-determined parameters, the TVP-VAR(p) process for all variance types is of lag order 3. Lastly, Table 4 shows that all markets for all variance types are significant at the 1% level for the ADF-test for stationarity. Therefore, all the assumptions required for the TVP-VAR(p) process hold for our dataset.

Having obtained all the necessary information for the TVP-VAR(3) model, it is estimated using the Gibbs Sampler with 22000 iterations, whereby the first 2000 iterations are discarded for convergence. The standard number of iterations is 11000, with the first 1000 iterations discarded (Raftery & Lewis, 1991), but due to the high number of parameters to be estimated, more iterations are required.

5.2 DAG structural results

The DAG-derived causal ordering of the contemporaneous shocks of the markets at a 1% significance level are displayed in Figure 1, applied to the residuals of the time-invariant VAR(3) models with RV_t, RS_t^+ and RS_t^-. For RV_t in Figure 1a, the exogenous shocks from all the markets seem to cause the shocks in SP500, whereas for RS_t^+ in Figure 1b, STO50 seems to be at the top of the hierarchy. For RS_t^- in Figure 1c, BTC is at the top of hierarchy, inferring negative volatility shocks all seem to transfer to the negative shocks in BTC. The linkage between ETH and BTC is bi-directional, which resembles the growing interdependence among cryptos as found by Koutmos (2018), as well as for N225 and STO50 at this significance level. But looking at the results of the negative shock transfer of RS_t^- in Figure 1c, it seems reasonable to assume that ETH shocks cause BTC shocks. In the same manner, by looking at the positive shocks for RS_t^+ in Figure 1b, N225 shocks seem to cause STO50 shocks, which is in line with the findings of Wang & Wu (2018), but for the time period 2002-2014.

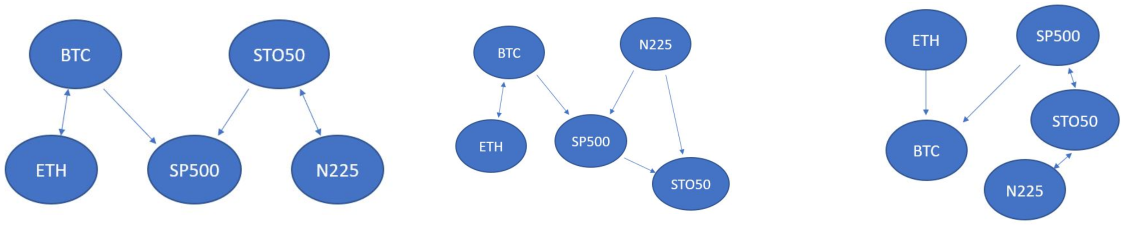

(a) DAG results for RV_t (b) DAG results for RS_t^+ (c) DAG results for RS_t^-

Figure 1: The DAG results for the residuals of a VAR(3) for RV_t, RS_t^+ and RS_t^-, at 1% significance level.

As discussed in the methodology, a more data-driven ordering of markets for the TVP-VAR(3) processes is preferred, even though the TVP-VAR(p) model was found to be empirically robust to different variable orderings (Primiceri, 2005). Considering the DAG structures above, along with subjective reasoning, the ordering of markets in (35) for RV_t seems to be most reasonable. The same ordering is applied for RS_t^+ and RS_t^+ as well.

$$RV_{1,t} : ETH \rightarrow RV_{2,t} : BTC \rightarrow RV_{3,t} : N225 \rightarrow RV_{4,t} : STO50 \rightarrow RV_{5,t} : SP500 \tag{35}$$

5.3 Orthogonalised impulse response functions results

The orthogonalised IRFs are implemented for all markets, based on exogenous shocks in a particular market on the days of its maximum variance. As the asymmetry analysis is left for FEVDs and the asymmetric spillover indices, the orthogonalised IRFs for only RV_t are shown in Figure 2, with the maximum variance dates for each market to be found in Table D.1 in the Appendix. The IRFs are scaled by the variance of the market itself, such that it can be simultaneously compared to each other. This means that a unit shock for the market in which the exogenous shock occured is visible at day 0, as well as contemporaneous responses of other markets to the unit shock. The unscaled orthogonalised IRFs can be found in Figures D.2-D.6 in the Appendix.

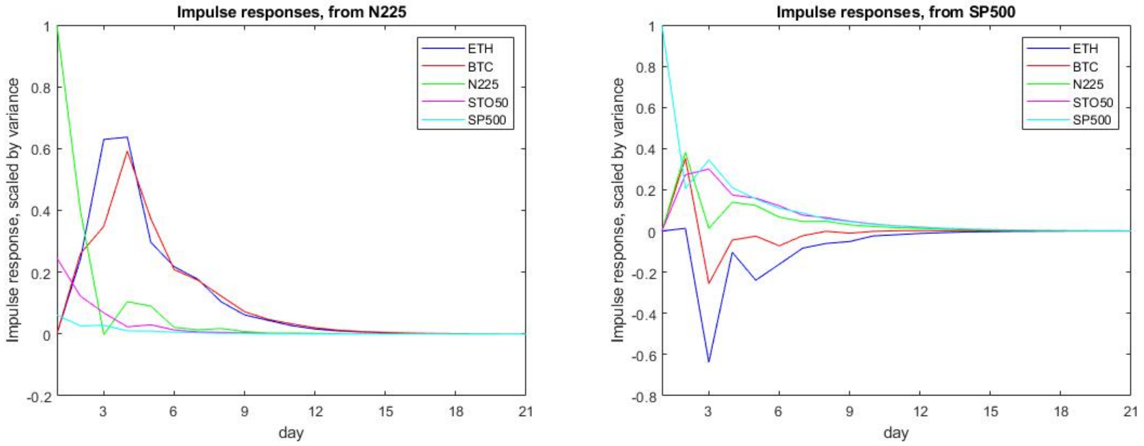

(a) From N225 shock (b) From SP500 shock

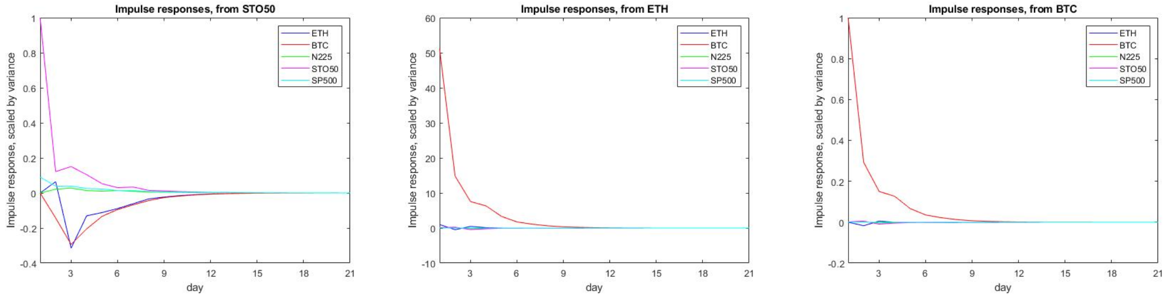

(c) From STO50 shock (d) From ETH shock (e) From BTC shock

Figure 2: The orthogonalised impulse responses of all markets, on an exogenous shock in a particular market on the day of its maximum variance, across a 21-day horizon.

The orthogonalised IRFs from shocks in N225, SP500 and STO50 are in Figures 2a, 2b and 2c respectively, with all IRFs performed in March 2020, as the highest variance of all markets is clearly due to the COVID-19 crisis' pessimistic market expectations. From an initial shock in N225, both STO50 and SP500 respond contemporaneously, by a scaled magnitude of 0.2 and 0.05 respectively. From a STO50 shock, only the SP500 has a contemporaneous response of about 0.1, whereas no market reacts immediately to an exogenous shock in SP500. This leads to all financial market responses to monotonically decrease after shocks in N225 and STO50, except after an SP500 shock, where STO50 and N225 initially respond positively up to 0.4 at day 3, eventually converging to 0 at day 9. Furthermore, both cryptos do not respond contemporaneously to shocks in any of the financial markets. Nevertheless, ETH and BTC have a relatively high positive response from a shock in N225, rising to 0.6 at day 3 but quickly converging back to 0 at day 12. For shocks in SP500 and STO50, both ETH and BTC react negatively, with maximally reaching -0.3 and -0.6 for shocks in STO50 and SP500 respectively at day 3 after the exogenous shock, but also quickly converging back to 0 at about day 9. The IRFs thus imply that cryptos are more influenced by shocks in N225 and SP500, rather than by STO50 shocks. This is of course due to cryptos also having been negatively affected by the COVID-19 crisis, but this can also be attributed to cryptos being most frequently traded in the Asian and North-American continent (Futures, 2018), thus more investors are exposed to volatility of both Asian/American financial- and crypto markets than investors in Europe.

The ETH and BTH orthogonalised IRFs can be seen in Figures 2d and 2e, with both maximum variances occuring on 2018/12/07. This time period is marked by BTC's mining difficulty being decreased due to power consumption concerns (Centieiro, 2019), consequently leading to major devaluations of BTC and ETH. A shock in ETH causes a contemporaneous shock in BTC with a magnitude of 50, much larger than any other market. The responses of the financial markets become unclear due to BTC's big response, but in Figure D.2 in the Appendix, the responses of the financial markets seem minimal. But with an initial shock in BTC, all markets, including ETH, seem to be immune to shocks coming from the BTC market, while BTC's response quickly declines to 0.2 after 3 days, eventually converging to 0 after 9 days. These IRFs seem to conclude that financial markets are unidirectionally connected to the crypto markets, in terms of volatility spillover, as ETH and BTC shocks do not seem to greatly impact financial markets, but this conclusion is also deemed logical, as the mining difficulty being dropped does not have any fundamental value for the financial markets.

5.4 Forecast error variance decomposition results

After the orthogonalised IRFs, the asymmetries among FEVDs for positive and negative semi-variances are explored. This was performed on the short-term 1-day, medium-term 10-day and long-term 30-day forecast horizons. As observed in the IRFs, all the responses on exogenous shocks die out after 9 to 12 days, which means that medium- and long-term FEVDs are practically indistinguishable from each other for all markets. Therefore, only the 1-day and 30-day horizon FEVDs are explored, with the 10-day horizon FEVDs to be found in Figures E.1-E.2 in the Appendix for all variance types.

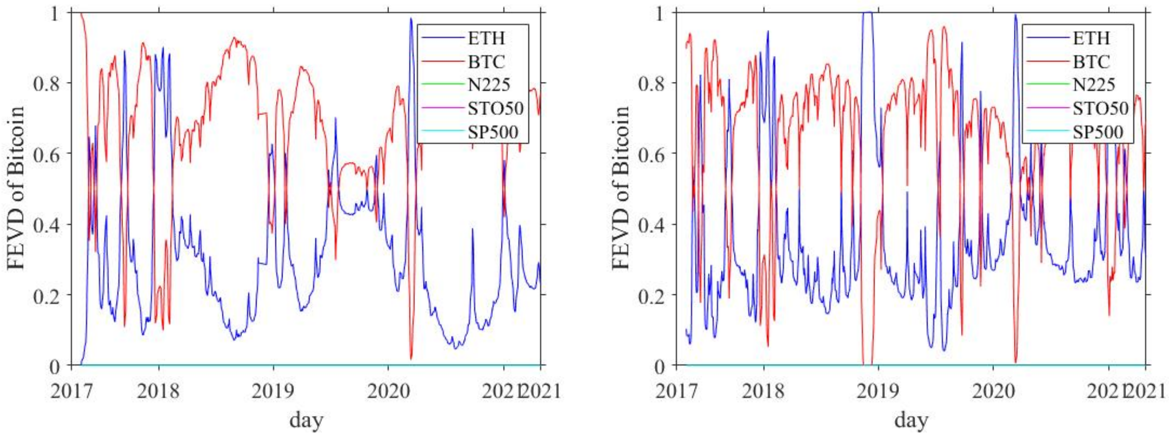

(a) FEVD of BTC for RS_t^+ (b) FEVD of BTC for RS_t^-

Figure 3: Forecast error variance decompositions of BTC for 1 day horizon for RS_t^+ and RS_t^-.

By exploring the 1-day FEVD horizon, more insights are gathered as to how innovations of markets affect the forecast error variance of a particular market contemporaneously, but also how the decompositions differ among positive and negative innovations. Figure 3 displays the FEVDs of BTC for the 1-day horizon. For all other markets, the fraction of variance explained by innovations in other markets is solely attributed to innovations of the market itself, which can be observed in Figures E.3 and E.4 in the Appendix. For BTC in contemporaneous times, only ETH and BTC innovations affect BTC's variance for both RS_t^+ and RS_t^-, reinforcing the findings of Koutmos (2018) of the high interconnectedness of cryptos. The findings for ETH do not resemble this interconnectedness, as due to the ordering of variables, ETH's variance can only be affected by exogenous shocks of itself in contemporaneous times.

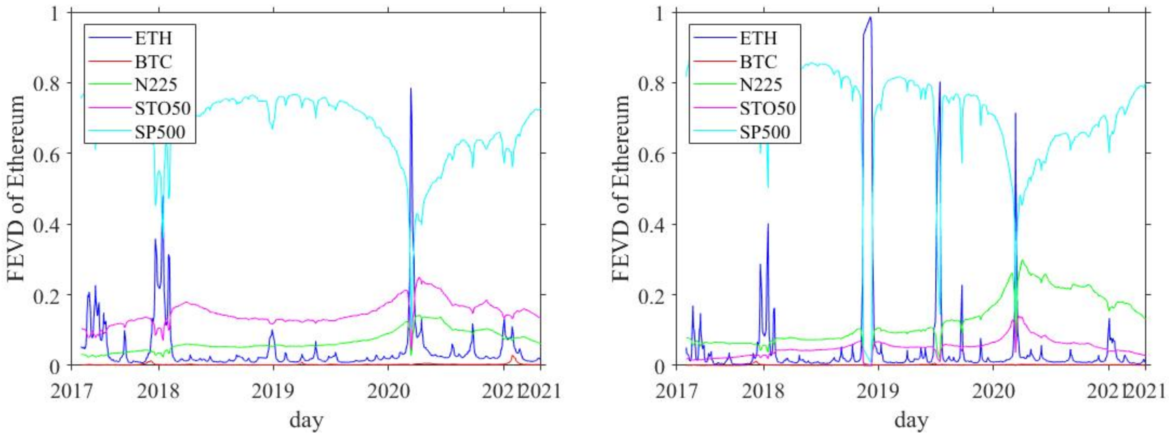

(a) FEVD of ETH for RS$_t^+$

(b) FEVD of ETH for RS$_t^-$

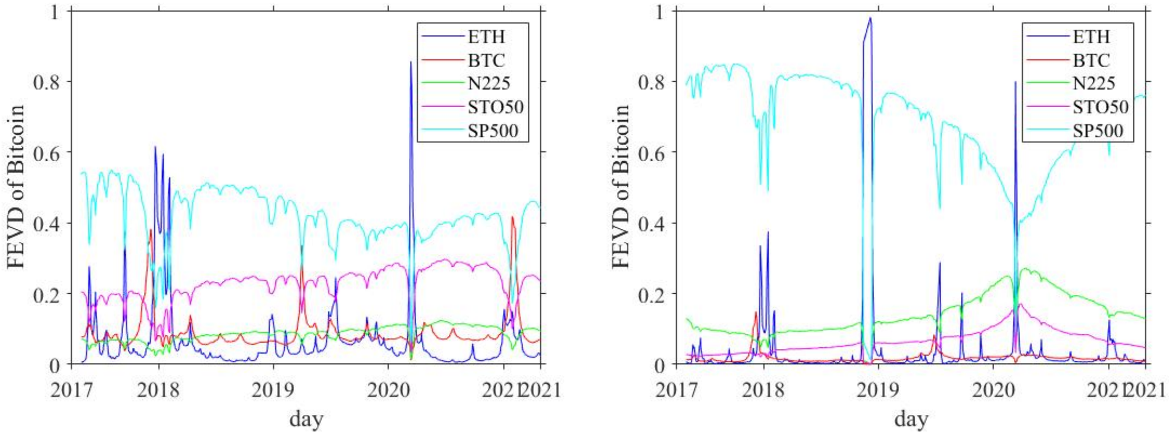

(c) FEVD of BTC for RS$_t^+$

(d) FEVD of BTC for RS$_t^-$

Figure 4: Forecast error variance decompositions of ETH and BTC for 30 day horizon for RS_t^+ and RS_t^-.

It is therefore more interesting the analyse the long-term FEVDs. Figure 4 displays the findings for ETH and BTC and Figure 5 for the financial markets for RS_t^+ and RS_t^-. Firstly, it can be noticed that innovations of SP500 explain most of the forecast error variance of all markets for both semivariances. Negative SP500 innovations seem to have a 10% larger effect on forecast error variances than positive SP500 innovations, which peaked during the COVID-19 crisis for the N225 and STO50 markets for RS_t^- in Figures 5b and 5d respectively. However, the fraction attributed to negative SP500 innovations drops significantly for ETH and BTC during the COVID-19 crisis, as negative ETH innovations seem to have emerged as the major source of variance for both cryptos during that time period. For positive semivariances, the fraction of SP500 innovations remains fairly constant over time.

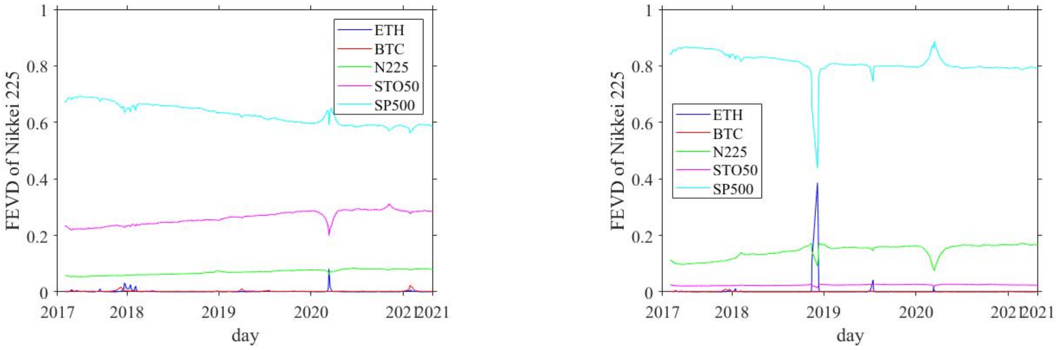

(a) FEVD of N225 for RS_t^+ (b) FEVD of N225 for RS_t^-

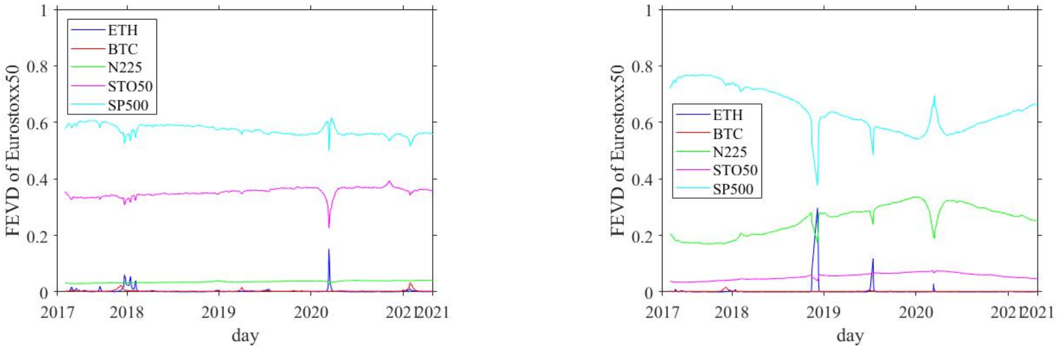

(c) FEVD of STO50 for RS_t^+ (d) FEVD of STO50 for RS_t^-

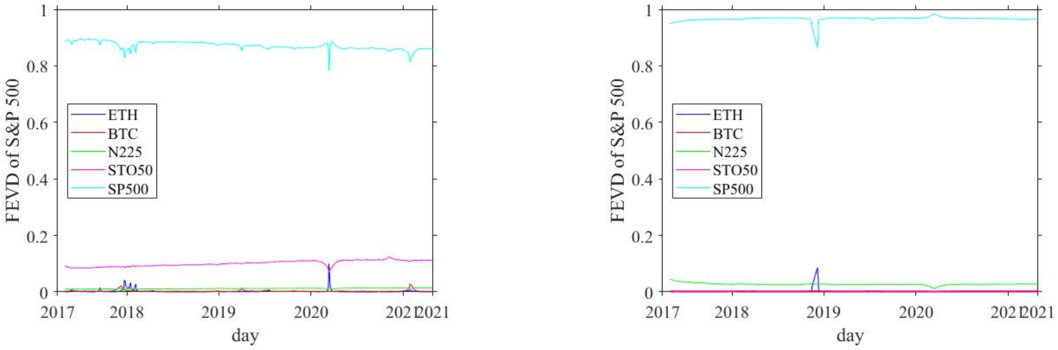

(e) FEVD of SP500 for RS_t^+ (f) FEVD of SP500 for RS_t^-

Figure 5: Forecast error variance decompositions of N225, STO50 and SP500 for 30 day horizon for RS_t^+ and RS_t^-.

In terms of ETH and BTC, it can be noted that innovations of both cryptos have a relatively small impact on the variances of the financial markets. It is interesting to see though that for all markets except BTC itself, BTC innovations for both semivariances have little to no impact. Even for its own market in Figures 4c and 4d, positive BTC innovations explain at most 40%

(beginning of 2021) of its own forecast error variance. For ETH, two things are noticeable: first, for the crypto markets, positive and negative ETH innovations suddenly explain a quite large fraction of the variance at the start of 2018 and then during the COVID-19 crisis, clearly related to the two major bear markets. Second, towards the end of 2018, only negative ETH innovations explain a significantly high fraction of all markets (see RHS sub-Figures of Figures 4 and 5), with the fractions in descending order from the cryptos, to N225, to STO50 and finally SP500. As with the orthogonalised IRFs, this activity is linked to the decreased mining difficulty of cryptos at the time, and clearly has a negative impact on all markets, though it is a short-lived peak in terms of forecast error variance explained.

The N225 and STO50 results in Figures 5a-5d, also show that FEVD asymmetries exist for such markets. Positive STO50 innovations have a 10% larger impact on forecast error variance for all markets than with negative STO50 innovations, though it is interesting to find that of all markets, the positive STO50 innovations bear the lowest fraction of variance explained for SP500. The reverse asymmetric results can be found for N225, as negative N225 innovations explain larger fractions of variances than with positive N225 innovations. Moreover, negative N225 innovations seem to affect crypto variances for RS_t^-, as can be seen in Figures 4b and 4d, more than N225 itself and SP500. As explained before, this is related to most of the cryptos being traded and mined in the Asian continent. In general, positive STO50 innovations explain more of the variance of all markets than positive N225 innovations. However, this pattern is reversed for negative semivariances, such that negative N225 innovations have a larger impact on the markets' variances.

5.5 Volatility spillover indices

As a follow-up on orthogonalised IRFs and FEVDs to study the asymmetries in the volatility transmission mechanism among the crypto- and financial markets, further understanding of the asymmetries can be obtained with several spillover indices, that are presented below for a 7-day horizon.

5.5.1 Total volatility spillover

Before focusing on the asymmetries of the volatility transmission mechanism, the connectedness of the crypto- and financial markets are studied, using the total volatility spillover index, derived with the time-varying coefficients of the TVP-VAR(3) process with RV_t. The realised variances of all markets, using the LHS y-axis, and the total volatility spillover index, using the RHS y-axis, is presented in Figure 6. Do note that the LHS y-axis is limited to the range between 0 and 0.1, as otherwise the extreme volatile periods for ETH and BTC at the end of 2018 and the COVID-19 crisis in 2020 hinder the visibility of the less volatile time periods. As described in the Data section, the two major bear markets at the start of 2018 and the COVID-19 crisis of

March 2020 are clearly visible due to the heightened realised variance of all markets, with the cryptos clearly displaying relatively higher volatility than the financial markets.

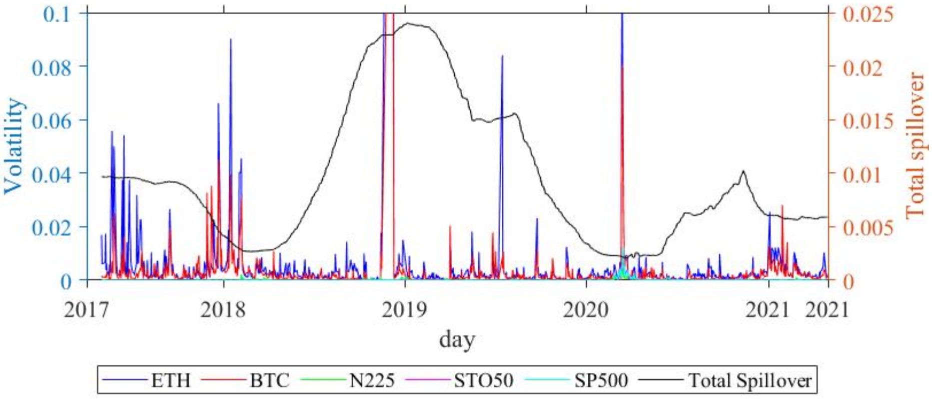

Figure 6: Plot of the total volatility spillover index and the realised variances of all markets.

The Figure shows that after major bear markets, the total spillover significantly increases, whereas during stable bull markets, the volatility transmission mechanism decreases. The total spillover index peaks at the start of 2019 at 0.024, and the second peak is observed in late 2020, at 0.01. Burns et al. (2012) argued that the financial crisis of 2008 altered the way market participants perceive risks, which led to a higher post-crisis connectedness of markets as investors homogenised market beliefs. This finding can also be found here for the time period 2017-2021 for the studied markets, as major downturns in one of the markets displays downturns in all other markets as well.

However, the total spillover index keeps rising until late 2019 after the bear market at the start of 2018. But after the COVID-19 crisis, the spillover index firstly keeps rising for a shorter time period. Secondly, the magnitude of this spillover increase is much lower. During the bear market of 2018, the crypto market bubble burst, where the crypto prices recovered only recovered the original level just in 2020. For the financial markets, SP500 and STO50 only recovered their original levels in late 2019, with N225 also just recovering before the COVID-19 crisis. This suggests that the total spillover mechanism rises when a stable market follows after a major bear market. However, with the COVID-19 crisis, the financial- and crypto markets quickly recovered and soared to all-time highs. Therefore, with such a quick-recovery bull market as in 2020, the total spillover index evidently does not rise as much.

5.5.2 Total spillover asymmetry measure

The focus is now to uncover the asymmetry of the volatility transmission mechanism, due to good and bad volatilities. The total spillover indices of RS_t^+ and RS_t^- over time are presented in Figure 7a, with the difference between these spillovers being represented by the total SAM in Figure 7b.

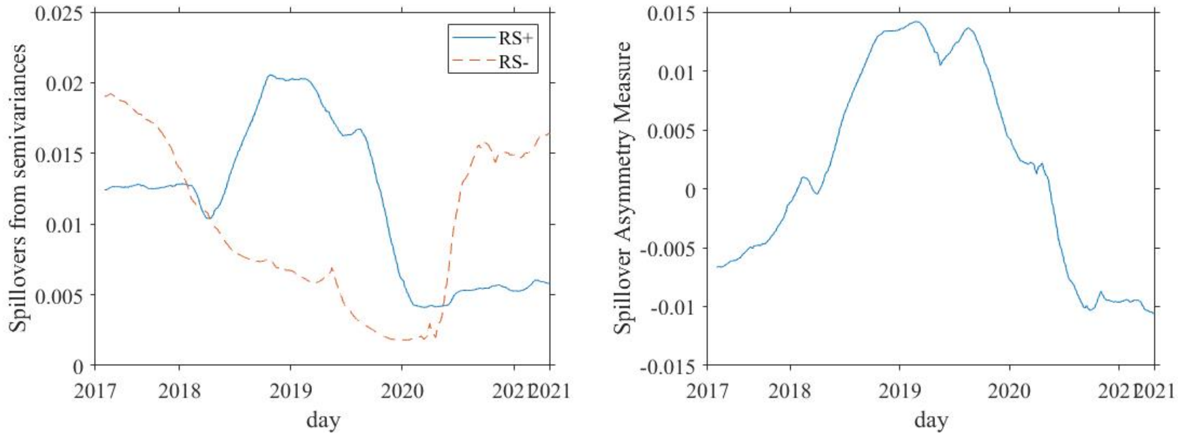

(a) Asymmetry spillover indices (b) Total SAM

Figure 7: Plots of the asymmetry spillover indices and the total SAM.

Between the two described bear markets, the good spillovers dominate the bad spillovers, inferring that there was optimism present in crypto- and financial markets. On the other hand, before the bear market of 2018 and after the COVID-19 crisis, the negative spillovers dominate, which seems immiment due to investors reacting to the bad news of the COVID-19 pandemic, and the corresponding pessimism that spread across the markets due to the higher volatility transmission mechanism at the time. It can be seen that negative spillovers monotonically decline between 2017 and February 2020, after which the negative spillovers quickly increase. In terms of the good spillovers, the 'small' bear market of 2018 decreases the good spillovers at the same rate as the negative spillovers. After February 2018, good spillovers rise to its highest level of the studied period at about 0.02, which resembles the rather stable financial period, in which clearly good rather than negative spillovers dominate. However, from mid-2019, the good spillovers decrease up until the COVID-19 crisis. This is in line with the decreasing total spillover index in Figure 6 over the same time frame, as it seems that markets become less interconnected due to optimistic market expectations, characterised by the stable bull market leading up to the COVID-19 crisis.

5.5.3 Spillover asymmetry measures from- and to markets

The total SAM can be further broken down to reveal asymmetries among the studied markets, by examining the contribution of individual markets towards asymmetry of the positive and negative volatility spillovers with SAM from a specific market i, $SAM^H_{i\rightarrow\bullet,t}$, and SAM to a specific market i, $SAM^H_{i\leftarrow\bullet,t}$. Figure 9 displays these SAM measures for the ETH and BTC markets, whereas the N225, STO50 and SP500 contributions are displayed in Figure 9.

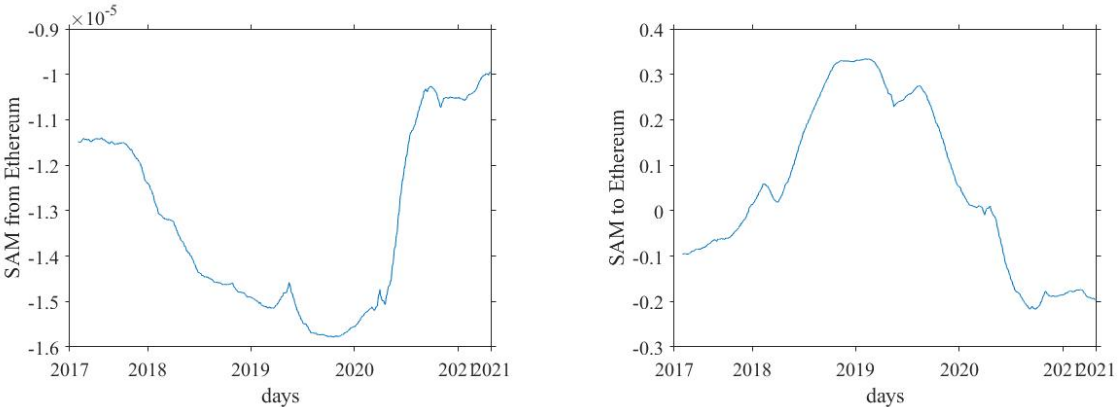

(a) SAM from Ethereum (b) SAM to Ethereum

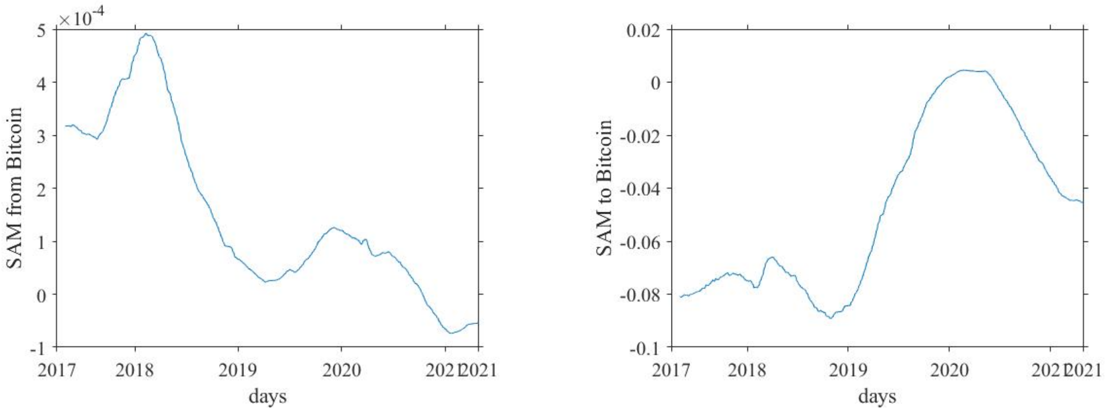

(c) SAM from Bitcoin (d) SAM to Bitcoin

Figure 8: Plots of the SAM from and to the ETH and BTC markets.

For ETH in Figures 8a and 8b, even though the difference between positive and negative spillovers is minimal, negative spillovers from ETH slightly dominate. The gap between positive and negative spillovers increases until 2020. After the COVID-19 crisis, positive spillovers quickly catch up with the negative spillovers, likely linked to the quick recovery of financial market after the crisis. Inversely, SAM to ETH seems very similar to the total SAM, by also observing a positive SAM in the period between the two major bear markets, likely transcending the positive spillovers from the financial markets. As stated with the total SAM, good rather than negative spillovers are more likely to transfer during financially stable time periods. For BTC in Figures 8c and 8d, the SAM from BTC is positive until mid-2020, clearly seeing that negative spillovers rose compared to positive spillovers due to the COVID-19 crisis. It can also be noted that after the Bitcoin crash at the start of 2018, the SAM from BTC monotonically decreases until mid-2019, suggesting that negative spillovers rose compared to positive spillovers, reflecting a more pessimistic view of crypto investors after the bear market of 2018. The SAM to BTC suggests that relatively more negative spillovers are transmitted from other markets.

Compared to the cryptos, financial markets reveal different results. The SAM from N225 and SP500 show that positive spillovers are decreasing the gap with negative spillovers, whereas SAM from SP500 grows from -0.1 to 0.3 and SAM from N225 also grows from -0.03 to 0.01.

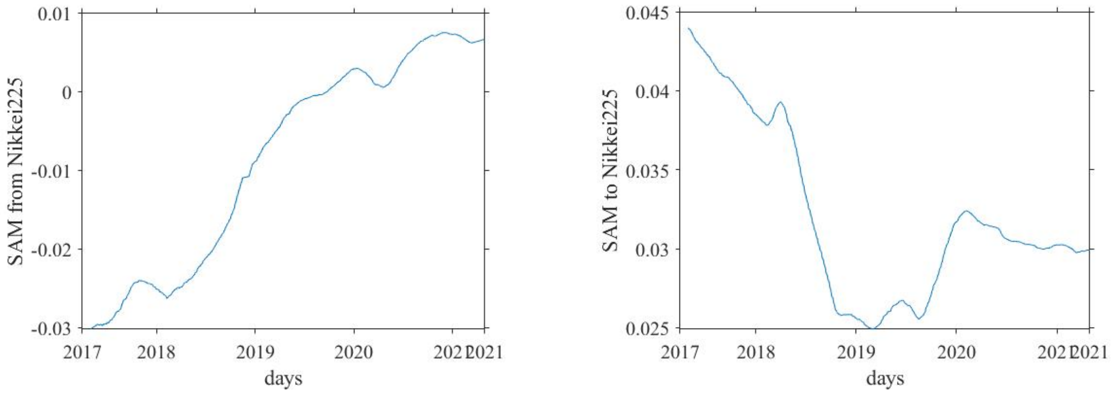

(a) SAM from Nikkei225 (b) SAM to Nikkei225

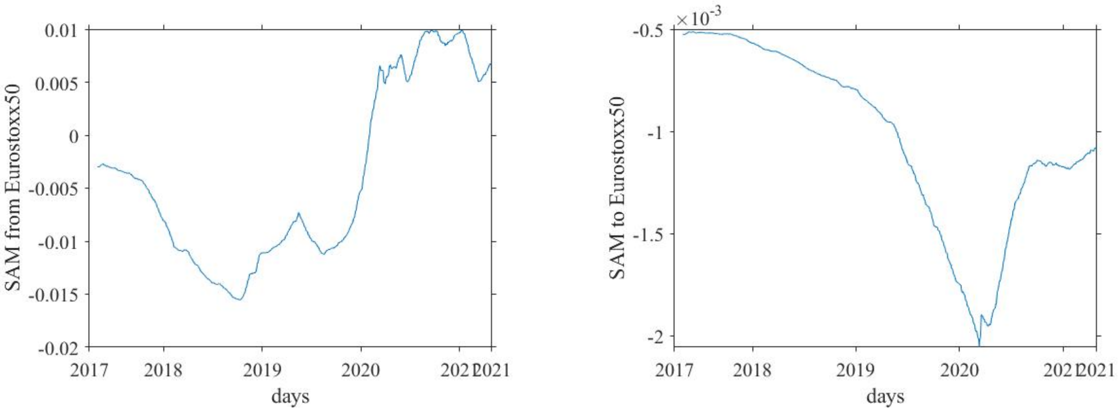

(c) SAM from Eurostoxx 50 (d) SAM to Eurostoxx 50

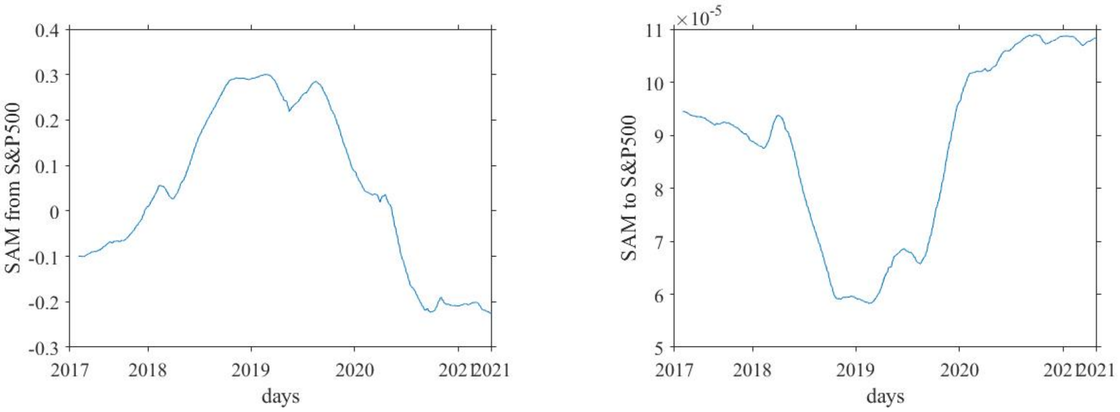

(e) SAM from S&P 500 (f) SAM to S&P 500

Figure 9: Plots of the SAM from and to the N225, STO50 and SP500 markets.

However, SAM from STO50 in Figure 9c shows that negative spillovers are becoming more dominant between 2017 and the end of 2018, after which SAM quickly rises to a positive level right before the COVID-19 crisis, eventually settling at a level of 0.01. Notice that the SAM from SP500 coincides with the total SAM in Figure 7b. This logically follows from the long-term FEVD results, where it is seen that SP500 innovations largely dominate the decomposition of forecast error variances of all markets, for both positive and negative semivariances. The other main difference is that negative spillovers, compared to good positive spillovers, from SP500 gain more ground than negative spillovers from the N225 and STO50 markets. This leads to a negative SAM from SP500 after the COVID-19 crisis, whereas the SAMs from N225 and STO50 actually becomes positive, likely due to the stock rally that is seen after the crisis. In terms of SAM to the financial markets in Figures 9b, 9d and 9f, due to the scale of SP500, any asymmetry in transmission of good and bad volatilities seems negligible. SAM to STO50 is also rather small in scale, but negative spillovers seem to slightly dominate positive spillovers entering the STO50 market across the whole time period, though it can be clearly seen that positive spillovers gain ground compared to negative spillovers during and after the COVID-19 crisis.

6 Conclusion and Discussion

The research question: *Are asymmetric volatility spillovers present between cryptocurrency and financial markets and how does this vary over time?* has been explored with the cryptocurrencies Bitcoin and Ethereum and the three major financial markets Nikkei 225, Eurostoxx 50 and S&P 500 between 2017 and 2021. The analysis is performed using a time-varying parameter VAR approach developed by Primiceri (2005) such that coefficients and variance-covariance matrices change at every time period, estimated using a Bayesian Gibbs Sampler method for realised variance RV_t, positive and negative semivariances, RS_t^+ and RS_t^-. The (asymmetric) volatility spillovers are quantified with a number of applications, as described below.

Firstly, the effect on other markets by an exogenous shocks in a specific market is studied using orthogonalised impulse response functions, in terms of RV_t. It is found that the financial markets are uni-directionally connected to the cryptos, as exogenous shocks in STO50 and SP500 initially create negative responses for ETH and BTC and positive responses for ETH and BTC from a shock in N225, but shocks in ETH and BTC do not impact the financial markets significantly. Secondly, forecast error variance decompositions are used to analyse the asymmetry in decomposition among good and bad volatilities using RS_t^+ and RS_t^-, based on 1-, 10- and 30-day forecasting horizons. For the 1-day horizon, most market variances are not influenced by other markets' innovations, except for the BTC market being affected by positive and negative innovations of ETH, as expected. For the 10- and 30-day horizons, positive and negative SP500 innovations are the biggest explanatory component for all markets' variance, though negative SP500 innovations explain a larger fraction of variances than positive SP500 innovations. Positive STO50 innovations explain larger fractions of forecast error variances than positive N225 innovations, however this relationship reverses for negative innovations. Moreover, it is surprising to see that BTC innovations have little to no impact on the variances of any of the markets, whereas ETH innovations are more prominent, especially with the negative innovations at the end of 2018, related to the mining difficulty of cryptos being reduced.

The volatility spillovers are then further studied using the total spillover index, which show that spillovers, thus the markets' connectedness, increase after major bear markets. However, total spillovers would not reach as high levels, when a quick recovery is seen after a bear market, which is seen after the COVID-19 crisis. This relates to the market connectedness increasing in times of crises and/or bear markets, whereby investors homogenise beliefs across different asset classes. This total spillover index is further disassembled into positive and negative spillovers due to RS_t^+ and RS_t^- respectively, through the SAM. As expected, the good spillovers dominate the bad spillovers between the two bear markets, inferring optimism in the crypto- and financial markets. But this reverses after the COVID-19 crisis, as negative spillovers dominate, which ties in with the reaction of investors to the bad news and market expectations at the time. Lastly, the contribution of each market towards the SAM is evaluated. For the main market SP500, good spillovers from SP500 to other markets dominate negative spillovers, until the COVID-19 crisis shows that relatively more negative spillovers from SP500 transfer to other markets. For SAM from N225 and STO50 though, both markets rise to a positive SAM level, thus relatively more positive spillovers are transferred to other markets after the COVID-19 crisis. For the cryptos, asymmetries in good and bad volatilities from ETH and BTC are minimal and rather see more volatility asymmetries receiving from all the other markets. This thus shows evidence that asymmetries in spillovers is uni-directional, mostly transferring to the crypto markets.

It can thus be concluded that asymmetric volatility spillovers among cryptocurrencies and financial markets indeed exist and that it varies over time dependent on the financial environment, as major bear markets clearly alter the dynamics of the volatility asymmetries, especially with the bear markets at the start of 2018 and the COVID-19 crisis. However, the extent of BTC's good and bad volatilities affecting volatilities in other markets is minimal, with ETH rather emerging as the crypto that is most interconnected with the financial markets.

The findings of this paper are interesting with regards to previous discoveries. Wang & Wu (2018) found that financial markets transmit more volatility to each other after major crises, which is also found in this paper after the bear markets of 2018 and the COVID-19 crisis. This finding is further enhanced by this paper, through differentiating for how volatility spillovers would continue to rise and to what extent the spillovers would increase. Wang & Wu (2018) also observed that SP500 explained the forecast error variance of good volatilities more than of bad volatilities between 2002-2014, while this paper discovers the reverse between 2017-2021. This paper also finds that both good and bad volatilities from the N225 market influence volatilities in ETH and BTC uni-directionally, though Malhotra & Gupta (2019) findings revealed that rather uni-directional spillovers from cryptos to major Asian Equity markets were present. Nevertheless, ETH and BTC still seem more interconnected with N225 and SP500 rather than STO50, likely due to these cryptos being most frequently traded in the Asian and American markets. Lastly, Wajdi et al. (2020) uncovered that bad rather than good volatilities are transmitted across cryptos. However, this paper finds evidence for the transmission of both semivariances, dependent on the time period, eg. positive volatilities between cryptos are notable during the two bear markets, whereas bad volatilities from ETH especially dominate at the end of 2018.

For future research, the following suggestions may give further insights in asymmetric volatility spillovers among crypto- and financial markets. First, the TVP-VAR model of Primiceri (2005) assumes the parameters vary at every time period, though no markets are found to have significant structural breaks at every single time period. Therefore, it would be interesting to review the results with the mixture innovation variant of the TVP-VAR model (Koop et al., 2009). Given that this model would only estimate new parameters and variance-covariance matrices at times when the structural break is significantly present, this would give insight as to whether the parameters of Primiceri's TVP-VAR are ill-determined or not. Second, even though Primiceri (2005) stated that the results from different orderings of variables is rather robust, contemporaneous results in orthogonalised IRFs and FEVDs are affected. For example, ETH is the most exogenous market and thus could not have been affected by innovations from other markets contemporaneously. Further research could overcome this problem by obtaining the average result from all the possible orderings of the markets. Last, the asymmetric volatility spillover indices are estimated using TVP-VAR models for positive and negative semivariances separately. By extending the model through including both positive and negative semivariances of all markets as endogenous variables, the transmission mechanism between good and bad volatilities across markets could then also be examined.

References

Andersen, T. G., Bollerslev, T., Diebold, F. X., & Ebens, H. (2001). The distribution of realized stock return volatility. *Journal of Financial Economics*, *61*(1), 43–76.

Barndorff-Nielsen, O. E., Kinnebrock, S., & Shephard, N. (2008). Measuring downside risk-realised semivariance. *CREATES Research Paper*(2008-42).

Baruník, J., Kočenda, E., & Vácha, L. (2016). Asymmetric connectedness on the us stock market: Bad and good volatility spillovers. *Journal of Financial Markets*, *27*, 55–78.

Baruník, J., Kočenda, E., & Vácha, L. (2017). Asymmetric volatility connectedness on the forex market. *Journal of International Money and Finance*, *77*, 39–56.

Bekaert, G., & Wu, G. (2000). Asymmetric volatility and risk in equity markets. *The Review of Financial Studies*, *13*(1), 1–42.

Bollerslev, T. (1986). Generalized autoregressive conditional heteroskedasticity. *Journal of Econometrics*, *31*(3), 307–327.

Brauneis, A., & Mestel, R. (2018). Price discovery of cryptocurrencies: Bitcoin and beyond. *Economics Letters*, *165*, 58–61.

Burns, W. J., Peters, E., & Slovic, P. (2012). Risk perception and the economic crisis: A longitudinal study of the trajectory of perceived risk. *Risk Analysis: An International Journal*, *32*(4), 659–677.

Carter, C. K., & Kohn, R. (1994). On gibbs sampling for state space models. *Biometrika*, *81*(3), 541–553.

Centieiro, H. (2019). What is happening to the bitcoin mining difficulty? *Henrique Centieiro*. `https://henriquecentieiro.medium.com/what-is-happening-to-the-bitcoin-mining-difficulty-c865f2bbb089`.

Chib, S., & Greenberg, E. (1995). Hierarchical analysis of sur models with extensions to correlated serial errors and time-varying parameter models. *Journal of Econometrics*, *68*(2), 339–360.

Chow, G. C. (1960). Tests of equality between sets of coefficients in two linear regressions. *Econometrica: Journal of the Econometric Society*, 591–605.

Cogley, T., & Sargent, T. J. (2005). Drifts and volatilities: monetary policies and outcomes in the post wwii us. *Review of Economic Dynamics*, *8*(2), 262–302.

Diebold, F. X., & Yılmaz, K. (2014). On the network topology of variance decompositions: Measuring the connectedness of financial firms. *Journal of Econometrics*, *182*(1), 119–134.

Elwood, S. K. (1997). Estimating permanent and transitory components of gnp using consumption information. *Southern Economic Journal*, 567–575.

French, K. R., Schwert, G. W., & Stambaugh, R. F. (1987). Expected stock returns and volatility. *Journal of Financial Economics*, *19*(1), 3.

Futures, F. (2018). Infographic: Which country trades the most bitcoin? *FINTECH FUTURES*. `https://www.fintechfutures.com/2018/08/infographic-which-country-trades-the-most-bitcoin/`.

Gkillas, K., & Katsiampa, P. (2018). An application of extreme value theory to cryptocurrencies. *Economics Letters*, *164*, 109–111.

Glosten, L. R., Jagannathan, R., & Runkle, D. E. (1993). On the relation between the expected value and the volatility of the nominal excess return on stocks. *The Journal of Finance*, *48*(5), 1779–1801.

Harvey, A., & Sucarrat, G. (2014). Egarch models with fat tails, skewness and leverage. *Computational Statistics & Data Analysis*, *76*, 320–338.

Hoover, K. D. (2005). Automatic inference of the contemporaneous causal order of a system of equations. *Econometric Theory*, *21*(1), 69–77.

Kalisch, M., & Bühlman, P. (2007). Estimating high-dimensional directed acyclic graphs with the pc-algorithm. *Journal of Machine Learning Research*, *8*(3).

Katrina, N. (2021). Tesla now accepts bitcoin as payment for cars, musk says. *Bloomberg*. `https://www.bloomberg.com/news/articles/2021-03-24/you-can-now-buy-a-tesla-with-bitcoin-elon-musk-says`.

Koop, G., & Korobilis, D. (2010). *Bayesian multivariate time series methods for empirical macroeconomics.* Now Publishers Inc.

Koop, G., Leon-Gonzalez, R., & Strachan, R. W. (2009). On the evolution of the monetary policy transmission mechanism. *Journal of Economic Dynamics and Control*, *33*(4), 997–1017.

Koutmos, D. (2018). Return and volatility spillovers among cryptocurrencies. *Economics Letters*, *173*, 122–127.

Lee, J., & Chinn, M. D. (1998). *The current account and the real exchange rate: A structural var analysis of major currencies.* National Bureau of Economic Research Cambridge, Mass., USA.

Liang, C. W., & Baig, T. (2021). Shifting cross-asset correlations. *DBS*. `https://www.dbs.com.hk/sme/aics/templatedata/article/generic/data/en/GR/052021/210525_insights_correlations.xml#`.

Lütkepohl, H. (2005). *New introduction to multiple time series analysis.* Springer Science & Business Media.

Malhotra, N., & Gupta, S. (2019). Volatility spillovers and correlation between cryptocurrencies and asian equity market. *International Journal of Economics and Financial Issues*, *9*(6), 208.

McKinney, W., et al. (2010). Data structures for statistical computing in python. In *Proceedings of the 9th python in science conference* (Vol. 445, pp. 51–56).

Phillips, D. (2020). Bitcoin investor lost $250,000 in hedge fund collapse. *Decrypt*. `https://decrypt.co/29656/bitcoin-investor-lost-250000-in-hedge-fund-collapse`.

Primiceri, G. E. (2005). Time varying structural vector autoregressions and monetary policy. *The Review of Economic Studies*, *72*(3), 821–852.

Raftery, A. E., & Lewis, S. (1991). *How many iterations in the gibbs sampler?* (Tech. Rep.). WASHINGTON UNIV SEATTLE DEPT OF STATISTICS.

Ross, S. A. (1989). Information and volatility: The no-arbitrage martingale approach to timing and resolution irrelevancy. *The Journal of Finance*, *44*(1), 1–17.

Seabold, S., & Perktold, J. (2010). statsmodels: Econometric and statistical modeling with python. In *9th python in science conference.*

Sims, C. (1993). *ka nine variable probabilistic macroeconomic forecasting model, lpp. 179" 204 in j. stock and m. watson, eds., business cycles indicators and forecasting.* University of Chicago Press for the NBER.

Sims, C. A. (1980). Macroeconomics and reality. *Econometrica: Journal of the Econometric Society*, 1–48.

Spirtes, P., Glymour, C. N., Scheines, R., & Heckerman, D. (2000). *Causation, prediction, and search.* MIT press.

Stein, F., Satpathy, N., Jacob, A., & Pavlov, N. (2020). Evaluating the performance of the beta-t-egarch and asymmetric garch against the vix for volatility forecasting.

Stock, J. H., & Watson, M. W. (1996). Evidence on structural instability in macroeconomic time series relations. *Journal of Business & Economic Statistics*, *14*(1), 11–30.

Swanson, N. R., & Granger, C. W. (1997). Impulse response functions based on a causal approach to residual orthogonalization in vector autoregressions. *Journal of the American Statistical Association*, *92*(437), 357–367.

van der Walt, S., Colbert, S. C., & Varoquaux, G. (2011). The numpy array: A structure for efficient numerical computation. *Computing in Science Engineering*, *13*(2), 22-30. doi: 10.1109/MCSE.2011.37

Van Rossum, G., & Drake Jr, F. L. (1995). *Python tutorial.* Centrum voor Wiskunde en Informatica Amsterdam, The Netherlands.

Wajdi, M., Nadia, B., & Ines, G. (2020). Asymmetric effect and dynamic relationships over the cryptocurrencies market. *Computers & Security*, *96*, 101860.

Wang, X., & Wu, C. (2018). Asymmetric volatility spillovers between crude oil and international financial markets. *Energy Economics*, *74*, 592–604.

Yang, J., & Zhou, Y. (2013). Credit risk spillovers among financial institutions around the global credit crisis: Firm-level evidence. *Management Science*, *59*(10), 2343–2359.

Yildirim, I. (2012). Bayesian inference: Gibbs sampling. *Technical Note, University of Rochester*.

Zhang, W., Wang, P., Li, X., & Shen, D. (2018). Some stylized facts of the cryptocurrency market. *Applied Economics*, *50*(55), 5950–5965.

Appendix A

Appendix A provides a description of all the scripts that are used to generate the results in this paper. All the scripts that are described below can be found within the *.zip* file, that is provided alongside this paper.

The data pre-processing and generating some of the results, such as generating realised variances, positive and negative semivariances, is performed in Python 3.5 (Van Rossum & Drake Jr, 1995) with the packages pandas (McKinney et al., 2010), numpy (van der Walt et al., 2011) and statsmodels (Seabold & Perktold, 2010). Two Python scripts are created named *TVP-VAR data preparation.py* and *Data characteristics.py*, which can be found in the folder *data generation (Python)* within the uploaded *.zip* file.

The script *TVP-VAR data preparation.py* is used to import the data for all the crypto- and financial markets that is required to obtain the realised variances, positive and negative semivariances. Then, the script *Data characteristics.py* is used to obtain the descriptive statistics, correlation matrices, the optimal lag order and stationarity tests for all the markets and variance types. The maximum variance for each market is also obtained in this script, alongside the day on which the maximum variance occurred.

After the data pre-processing in Python, the rest of the results are obtained in Matlab. As mentioned in the methodology, the TVP-VAR model is run using the code provided by Koop & Korobilis (2010), with adaptations such that all the results can be obtained, as listed below. The following scripts and functions are created:

- *main.m*: this is the main script, which uses all the below-listed functions/scripts. It runs the TVP-VAR model for every variance type. Then, it creates all the required figures which are used in this paper, such as impulse responses, forecast error variance decompositions over time and all the (asymmetric) spillover indices.
- *structural_break_counts.m*: this script counts the number of structural breaks that are significant, using the Chow test for every market and variance type.
- *hetero_TVP_VAR_func.m*: runs the heteroskedastic TVP-VAR model, as provided by Koop & Korobilis (2010) (by heteroskedasticity is meant that the variance-covariance matrix is also time-varying). The parameters are estimated using the Gibbs sampler, after which the posterior means of the parameters, impulse responses and forecast error variance decompositions (FEVD) of all the draws are calculated. This function then outputs the estimated coefficient matrices, the impulse responses and the FEVDs. Lastly, it also creates the figures for the impulse responses, both the scaled and the unscaled versions (which includes the 16th and 84th quantile, representing the confidence interval).

- *ts_prior.m*: extracts the parameters required for the initialisation of the prior conditional distributions, as described in subsection 3.3.3.
- *quantile.m*: This function obtains the xth quantile of a certain vector. This is especially used when the posterior means of all the estimated parameters are calculated in the Gibbs sampler and extracting the 16th and 84th quantiles of the impulse responses.
- *IRA_tvp.m*: this script generates the impulse responses at every draw of the Gibbs sampler for the given dates, based on the maximum variance of the studied markets. Furthermore, the forecast error variance decompositions are also calculated for every time period.
- *mlag2.m*: given Y as input matrix, it creates the lagged Y matrix, based on the lag order of the TVP-VAR model. if Y is a TxN matrix, where T stands for the number of observations and N for the number of parameters, then lagged Y would be a Tx(Np) matrix, where p represents the lag order of the TVP-VAR model.
- *draw_sigma.m*: within the Gibbs sampler, this function draws the elements of D_t, the diagonal matrix.
- *SVRW2.m*: this function is responsible for drawing the stochastic volatility, which is used to draw the elements of D_t.
- *draw_alpha.m*: within the Gibbs sampler, this function draws the elements of ϕ_t, the lower triangular matrix with ones on the diagonal positions.
- *draw_beta.m*: within the Gibbs sampler, this function draws the elements of $A_{p,t}$, the coefficient matrix of the pth lag order at time t.
- *wish.m*: extracts observations from the Wishart distribution, with scale matrix h and degrees of freedom being ν, using Bartlett's decomposition. Observations from the Wishart distribution are needed to make draws of the hyperparameters of V, from (10), which all follow an inverse-Wishart distribution as described in subsection 3.3.3.
- *corrvc.m*: this function computes the correlation matrix from the variance-covariance matrix. This function is used when deriving the time-varying variance-covariance matrix at every draw of the Gibbs sampler.
- *carter_kohn.m*: this script provides the Kalman filter (see Carter & Kohn (1994) for more details on the Kalman filter) and the backward recursion, which are required to calculate all the observations of a certain parameter, within a draw of the Gibbs sampler.
- *mvnrnd.m*: this function generates a matrix of random numbers, with a predetermined length, from a multivariate normal distribution that has mean μ and variance-covariance matrix Σ. This is especially used within the scripts *draw_alpha.m* and *draw_beta.m*, when draws of these matrices are taken from the conditional posterior distribution.

- *create_fevd_figures.m*: this function creates the figures of the forecast error variance decompositions of all markets for the 1-day, 10-day and 30-day horizons.
- *get_spillovers_indices.m*: this function calculates the total spillover index and also the contribution of individual markets to this total volatility spillover. This is done by determining the volatility spillover from a specific market to all the other markets, but also the volatility spillovers from all markets to a specific market.
- *create_spillover_figures_tomarkets.m*: This function creates the figures for SAM to a specific market, with volatility spillovers coming from all the other markets.
- *create_spillover_figures_frommarkets.m*: this function creates the figures for SAM from a specific market, with the volatility spillover going to all other markets. Separate functions are created for SAM from- and to markets, such that the figures have the correct titles and labelling.

Appendix B

B.1: Sample drawing of ϕ^T

To understand why samples of ϕ^T cannot be drawn as easily as with α^T, we use the original representation of the TVP-VAR(p) model:

$$RV_t = c_t + A_{1,t}RV_{t-1} + \ldots + A_{p,t}RV_{t-p} + \epsilon_t \tag{36}$$

As defined in the methodology, the residual variance-covariance matrix, $\Sigma_{\epsilon,t} = F_tD_tF_t'$, where F_t is a lower triangular matrix with ones on the diagonal and D_t a diagonal matrix at time t, as below:

$$F_t = \begin{bmatrix} 1 & 0 & \ldots & 0 \\ \phi_{21,t} & 1 & \ddots & \vdots \\ \vdots & \ddots & \ddots & 0 \\ \phi_{N1,t} & \ldots & \phi_{NN-1,t} & 1 \end{bmatrix}, D_t = \begin{bmatrix} \sigma_{1,t} & 0 & \ldots & 0 \\ 0 & \sigma_{2,t} & \ddots & \vdots \\ \vdots & \ddots & \ddots & 0 \\ 0 & \ldots & 0 & \sigma_{N,t} \end{bmatrix} \tag{37}$$

By using F_t and D_t, it follows from (36) that the TVP-VAR process can be rewritten to (38). By stacking the coefficient matrices through a vectorisation process of all the ith lagged coefficient matrices on the right hand side (RHS) of the equation, it can be further condensed into (39), where $\otimes$ denotes the Kronecker product.

$$RV_t = c_t + A_{1,t}RV_{t-1} + \ldots + A_{p,t}RV_{t-p} + A_t^{-1}\Sigma_t u_t \ \ , \ where \ V(u_t) = I_N. \tag{38}$$

$$RV_t = X_t'A_t + A_t^{-1}\Sigma_t u_t \ \ , \ where \ X_t = I_N \otimes [1, RV_{t-1}', \ldots, RV_{t-p}']. \tag{39}$$

The system of equations in (39) is then further manipulated as seen below in (40), where $\hat{RV}_t$ is observable when A^T is given (which is the case as we would draw A^T before drawing ϕ^T in the Gibbs Sampler). Given that F_t is a lower triangular matrix with ones on the diagonal, (40) can be further condensed, as in (41), where ϕ_t is the same as in (8) such that it is a $(\frac{N(N-1)}{2})$x1 vector of non-zero and non-one elements of the rows of the matrix F_t^{-1} and Z_t is a N x $\frac{N(N-1)}{2}$ matrix, denoted by (42). the notation $\hat{RV}_{[1,..,i]}, t$ in Z_t represents the row vector $[\hat{RV}_{1,t}, \hat{RV}_{2,t}, \ldots, \hat{RV}_{i,t}]$.

$$F_t(RV_t - X_t'A_t) = F_t\hat{RV}_t = D_tu_t. \quad (40) \qquad\qquad \hat{RV}_t = Z_t\phi_t + D_tu_t \quad (41)$$

$$Z_t = \begin{bmatrix} 0 & \ldots & \ldots & 0 \\ -\hat{RV}_{1,t} & 0 & \ldots & 0 \\ 0 & -\hat{RV}_{[1,2],t} & \ddots & \vdots \\ \vdots & \ddots & \ddots & 0 \\ 0 & \ldots & 0 & -\hat{RV}_{[1,..,N-1],t} \end{bmatrix} \tag{42}$$

From (41), it becomes evident that the model has a nonlinear Gaussian representation, through the time-varying coefficient at every time t. However, the problem is that the observable $\hat{RV}_t$ appears on both the LHS and RHS (in Z_t) of the equation. This means that $[\hat{RV}_t,\ \hat{\phi}_t]$ are not jointly normal, implying that the conditional distributions also cannot be derived using the normal Kalman filter recursion, as with α^T. But by having the additional assumption of Ψ, the variance of the residual from the random walk model of ϕ_t, being block diagonal, the matrices can be broken down equation by equation, on which the Kalman filter and the backward recursion can be applied. There are two reasons why this works: First, the endogenous variable of the ith market's equation, $\hat{RV}_{i,t}$ is not on the RHS of the same equation anymore. Second, the row vector $\hat{RV}_{[1,\ldots,i-1],t}$ becomes predetermined in the ith equation, as the endogenous variable vector for i<k for the kth equation would be recursively derived before.

As explained in the methodology, this allows us to decompose ϕ^T equation by equation, where $\phi_{i,t}$ represents the ith block of ϕ_t that corresponds with the ith equation's coefficients in (41). $\phi_{i,t}$ can be recursively drawn from the Gaussian distribution $p(\phi_{i,t}|\phi_{i,t+1}, RV^t, \alpha^T, \sigma^T, V)$ $\sim N(a_{i,t|t+1}, \nu_{i,t|t+1})$, where $a_{i,t|t+1} = E(\phi_{i,t}|\phi_{i,t|t+1}, RV^t, \alpha^T, \sigma^T, V)$ and $\nu_{i,t|t+1} = Var(\phi_{i,t}|\phi_{i,t|t+1}, RV^t, \alpha^T, \sigma^T, V)$ for the ith equation.

B.2: Rewriting a TVP-VAR(p) process into a TVP-VAR(1) process

For orthogonalised IRFs and FEVDs, it is useful to rewrite the TVP-VAR(p) process (as can be seen in (43)) as a TVP-VAR(1) process (as can be seen in (44)). In terms of the inputs, the TVP-VAR(p) process has RV_t and ϵ_t as Nx1 vectors of the endogenous variables and the residuals respectively at time t and $A_{i,t}$ as the NxN coefficient matrix of the ith lag at time t. The vectors and matrices are different for the TVP-VAR(1) process, where $\boldsymbol{RV}_t$ is an Npx1 vector of the endogenous variables of the p lagged observations stacked up one below the other, $\boldsymbol{e}_t$ is an Npx1 vector of residuals where only the first N elements are the elements of ϵ_t and zero otherwise and $\boldsymbol{A}_t$ is an NpxNp coefficient matrix, where the first N rows contain the coefficient matrices $A_{i,t}$ from the TVP-VAR(p) process, the lower-left N(p-1)xN(p-1) block of the matrix has NxN identity matrices on the diagonal and the last N columns of the lower N(p-1) rows only contain zeros.

$$RV_t = \mu_t + \sum_{i=1}^{p} A_{i,t} RV_{t-i} + \epsilon_t \tag{43}$$

$$\boldsymbol{RV_t} = \boldsymbol{A_t}\boldsymbol{RV_{t-1}} + \boldsymbol{e_t}, \text{where } \boldsymbol{RV_t} = \begin{pmatrix} RV_t \\ \vdots \\ RV_{t-p+1} \end{pmatrix}, \boldsymbol{e_t} = \begin{pmatrix} \epsilon_t \\ 0 \\ \vdots \\ 0 \end{pmatrix}, \boldsymbol{A_t} = \begin{pmatrix} A_{1,t} & \ldots & A_{p-1,t} & A_{p,t} \\ I_N & \ldots & 0 & 0 \\ \vdots & \ddots & \vdots & \vdots \\ 0 & \ldots & I_N & 0 \end{pmatrix} \tag{44}$$

To show that both TVP-VAR processes are equivalent, example vectors and matrices of the TVP-VAR(1) process are presented below using the optimal lag order used in this paper, p=3:

$$\boldsymbol{RV_t} = \begin{pmatrix} RV_t \\ RV_{t-1} \\ RV_{t-2} \end{pmatrix}, \boldsymbol{e_t} = \begin{pmatrix} \epsilon_t \\ 0 \\ 0 \end{pmatrix}, \boldsymbol{A_t} = \begin{pmatrix} A_{1,t} & A_{2,t} & A_{3,t} \\ I_N & 0 & 0 \\ 0 & I_N & 0 \end{pmatrix} \tag{45}$$

By inputting these vectors and matrices into (44) and multiplying everything out, it can be seen below that the first N rows become the TVP-VAR(p) process $RV_t = \sum_{i=1}^{p} A_{i,t}RV_{t-i} + \epsilon_t$ and the remaining N(p-1) rows show that the lagged RV_{t-i} for i=1,2 are equal to itself. Therefore, both TVP-VAR representations are equivalent.

$$\begin{pmatrix} RV_t \\ RV_{t-1} \\ RV_{t-2} \end{pmatrix} = \begin{pmatrix} A_{1,t} & A_{2,t} & A_{3,t} \\ I_N & 0 & 0 \\ 0 & I_N & 0 \end{pmatrix} \begin{pmatrix} RV_{t-1} \\ RV_{t-2} \\ RV_{t-3} \end{pmatrix} + \begin{pmatrix} \epsilon_t \\ 0 \\ 0 \end{pmatrix} = \begin{pmatrix} A_{1,t}RV_{t-1} + A_{2,t}RV_{t-2} + A_{3,t}RV_{t-3} + \epsilon_t \\ RV_{t-1} \\ RV_{t-2} \end{pmatrix} \tag{46}$$

B.3: Derivation of the orthogonalised impulse response functions

This section follows Lütkepohl (2005) and elaborates as to why the orthogonalised impulse responses, for a certain time horizon H, are denoted by $\Theta_{i,t}$ of the orthogonalised MA representation of the TVP-VAR(p) process:

$$\Theta_{0,t} = P_t \quad , \quad \Theta_{1,t} = \Phi_{1,t}P_t \quad , \quad \ldots \quad , \quad \Theta_{H,t} = \Phi_{H,t}P_t. \tag{47}$$

First, consider the zero mean TVP-VAR(p) model:

$$RV_t = A_{1,t}RV_{t-1} + \ldots + A_{p,t}RV_{t-p} + \epsilon_t \tag{48}$$

This model can be rewritten such that the residuals of the equations related to the different markets are independent of each other. Therefore, a decomposition of the residual variance-covariance matrix $\Sigma_{\epsilon,t} = F_tD_tF_t'$ is chosen, where F_t is lower triangular with ones on the diagonal, D_t a diagonal matrix at time t. This can be obtained from the Cholesky decomposition, $\Sigma_{\epsilon,t} = P_tP_t'$, where P_t is a lower triangular matrix. By establishing a diagonal matrix Δ_t, where the diagonal elements are equivalent to the diagonal elements of P_t, F_t and D_t can be specified as follows: $F_t = P_t\Delta_t^{-1}$ and $D_t = \Delta_t\Delta_t'$. By pre-multiplying (36) with $B_t = F_t^{-1}$, it provides

$$B_tRV_t = A_{1,t}^{*}RV_{t-1} + \ldots + A_{1,p}^{*}RV_{t-p} + u_t, \tag{49}$$

where $A_{i,t}^{*} = B_tA_{i,t}$ for all t and i = 1, ..., p and $u_t = (u_{1,t}, ..., u_{N,t}) = B_t\epsilon_t$. It then follows that u_t has a diagonal variance-covariance matrix $\Sigma_{u,t} = E(u_tu_t') = B_tE(\epsilon_t\epsilon_t')B_t' = B_t\Sigma_{\epsilon,t}B_t'$. Next, by adding $(I_N - B_t)RV_t$ on each side of (49) gives (50), where $A_{0,t}^{*} = I_N - B_t$. As previously defined, F_t is a lower triangular matrix with ones on the diagonal. This then also indicates that B_t should be lower triangular. Therefore, $A_{0,t}^{*}$ becomes the lower triangular matrix as described in (51), with the diagonal elements becoming zero.

$$RV_t = A^*_{0,t} RV_t + A^*_{1,t} RV_{t-1} + \ldots + A^*_{p,t} RV_{t-p} + u_t \tag{50}$$

$$A^*_{0,t} = \begin{bmatrix} 0 & 0 & \ldots & 0 & 0 \\ a^*_{21,t} & 0 & \ldots & 0 & 0 \\ \vdots & \ddots & \ddots & & \vdots \\ \vdots & & \ddots & \ddots & \vdots \\ a^*_{N1,t} & a^*_{N2,t} & \ldots & a^*_{N(N-1),t} & 0 \end{bmatrix} \tag{51}$$

As can be seen in (51), the first row, or the equation corresponding to the first market, does not contain any non-zero elements. To interpret it in terms of a TVP-VAR(p) process, this means that the first equation does not have any instantaneous RVs on the RHS. To generalise it for the kth equation, it can only contain instantaneous $RV_{i,t}$ for i<k. By recursively tracking $u_{i,t}$, the innovation of the ith market at time t with a size of one standard error, the $\Theta_{i,t}$, which is the coefficient matrix from the orthogonalised MA representation of a TVP-VAR(p) model, becomes the impulse response. This can be concluded, if the system in (50) is solved for RV_t, by pre-multiplying both sides by $(I_N - A^*_{0,t})^{-1}$:

$$RV_t = (I_N - A^*_{0,t})^{-1} A^*_{1,t} RV_{t-1} + \ldots + (I_N - A^*_{0,t})^{-1} A^*_{p,t} RV_{t-p} + (I_N - A^*_{0,t})^{-1} u_t \tag{52}$$

Notice that $(I_N - A^*_{0,t})^{-1} = F_t = P_t \Delta_t^{-1}$. This shows that the responses to a one standard deviation exogenous shock in a particular market is shown by $F_t \Delta_t = P_t = \Theta_{0,t}$, due to the diagonal elements of Δ_t being the standard deviations of u_t. The $\Theta_{i,t}$s are then recursively calculated using $\Phi_{i,t}$, being the coefficient matrix of the normal MA representation of the TVP-VAR(p) process at the ith time horizon within the impulse response horizon h.

Appendix C

Table C.1: The correlation matrix of all markets with RS_t^+ and RS_t^-

	RS_t^+					RS_t^-				
Markets	ETH	BTC	N225	STO50	SP500	ETH	BTC	N225	STO50	SP500
ETH	1.000					1.000				
BTC	0.603	1.000				0.929	1.000			
N225	0.108	0.137	1.000			0.075	0.115	1.000		
STO50	0.159	0.235	0.555	1.000		0.069	0.107	0.489	1.000	
SP500	0.225	0.359	0.525	0.771	1.000	0.079	0.121	0.286	0.741	1.000

Appendix D

Table D.1: The dates at which the maximum variance of all markets is noted, for RV_t

Market	**Date of maximum variance**	**Maximum variance**
ETH	2018/12/07	0.4271
BTC	2018/12/07	0.2379
N225	2020/03/13	0.0068
STO50	2020/03/16	0.0095
SP500	2020/03/16	0.0123

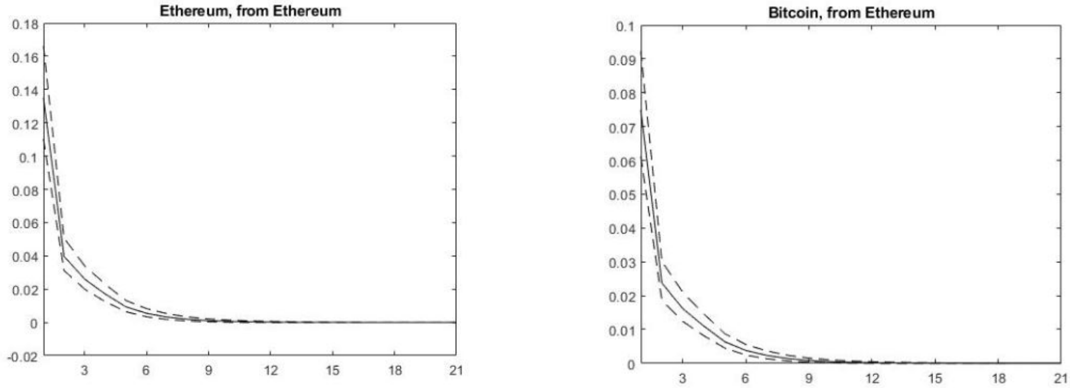

(a) Response of ETH, from ETH (b) Response of BTC, from ETH

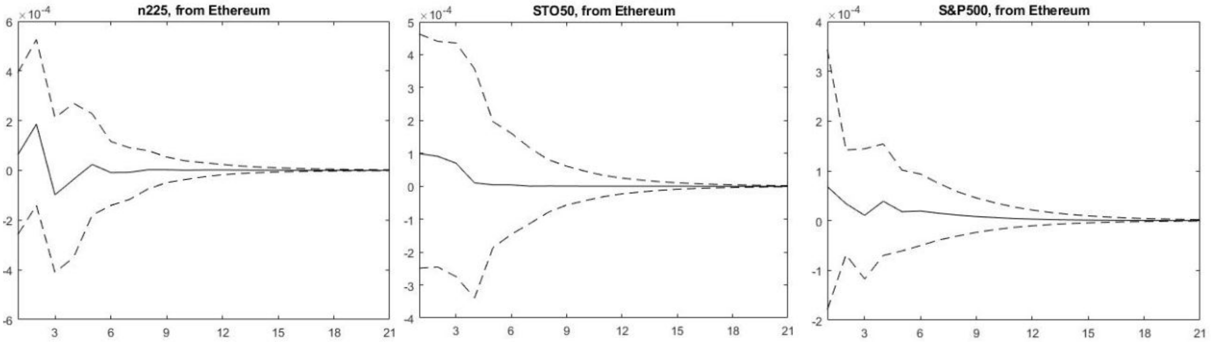

(c) Response of N225, from ETH (d) Response of STO50, from ETH (e) Response of SP500, from ETH

Figure D.2: Orthogonalised impulse response functions, from an exogenous shock in Ethereum, with the 16th and 84th quantiles.

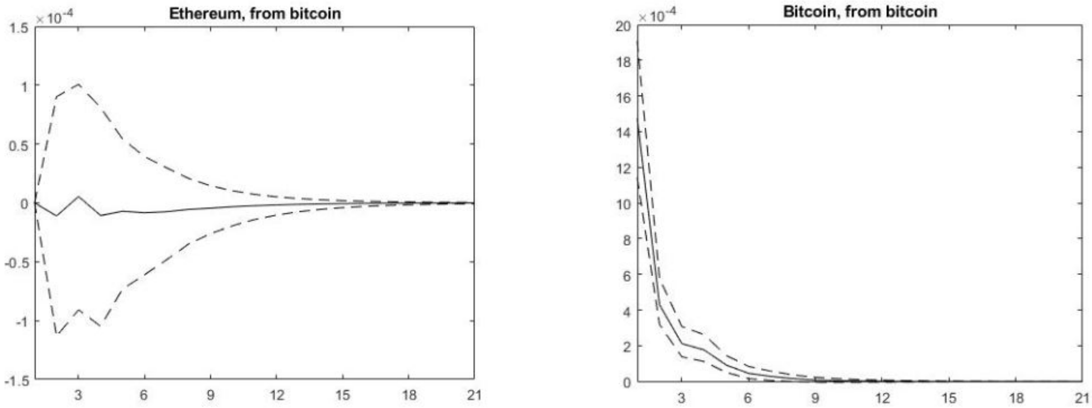

(a) Response of ETH, from BTC (b) Response of BTC, from BTC

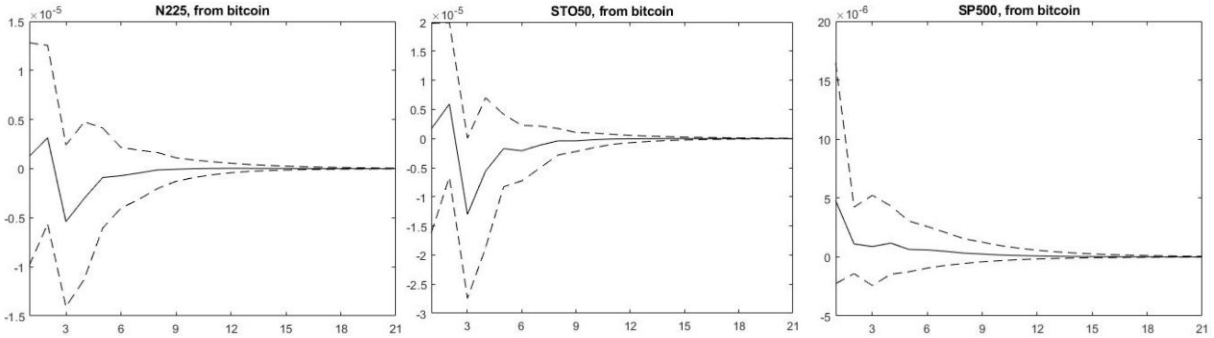

(c) Response of N225, from BTC (d) Response of STO50, from BTC (e) Response of SP500, from BTC
Figure D.3: Orthogonalised impulse response functions, from an exogenous shock in Bitcoin, with the 16th and 84th quantiles.

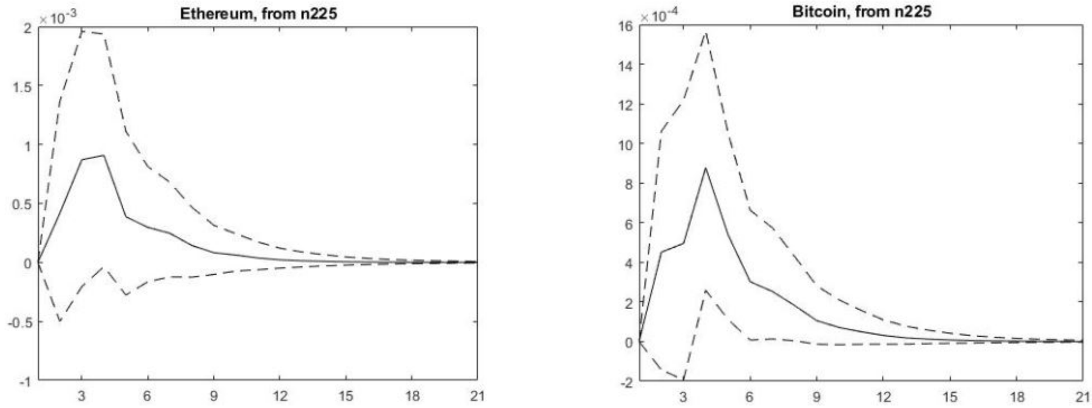

(a) Response of ETH, from N225 (b) Response of BTC, from N225

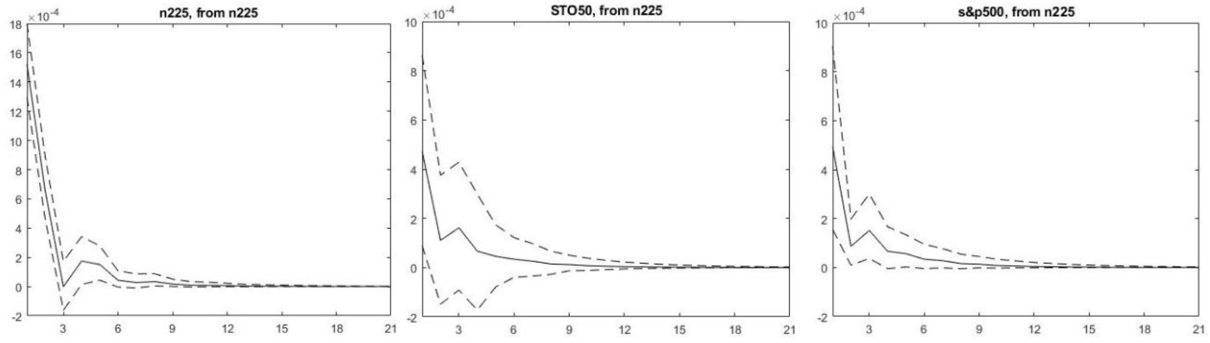

(c) Response of N225, from N225 (d) Response of STO50, from N225 (e) Response of SP500, from N225
Figure D.4: Orthogonalised impulse response functions, from an exogenous shock in Nikkei225, with the 16th and 84th quantiles.

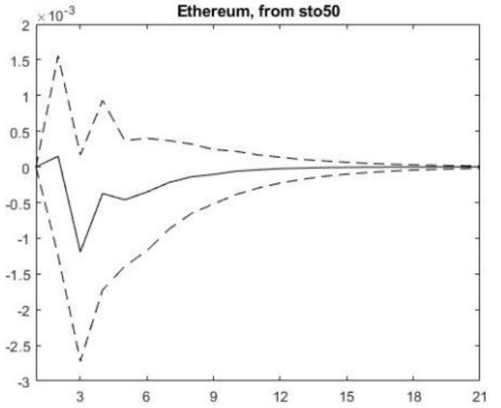

(a) Response of ETH, from STO50 (b) Response of BTC, from STO50

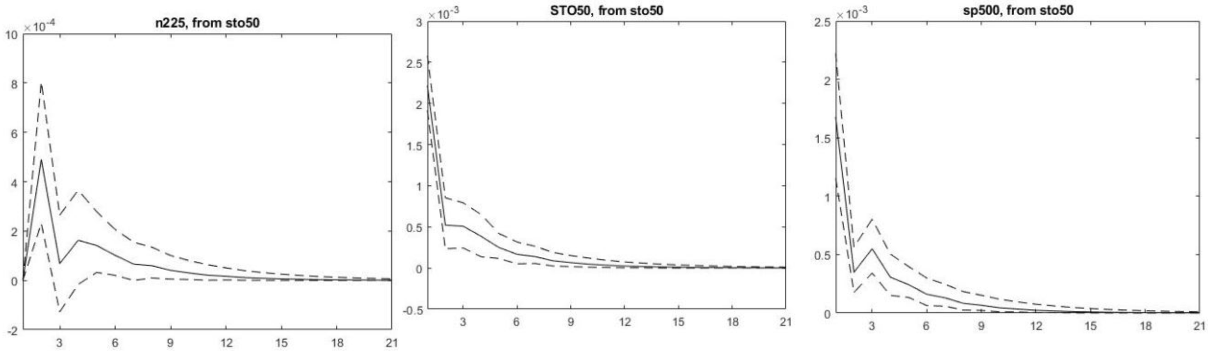

(c) Response of N225, from STO50 (d) Response of STO50, from STO50 (e) Response of SP500, from STO50

Figure D.5: Orthogonalised impulse response functions, from an exogenous shock in Eurostoxx 50, with the 16th and 84th quantiles.

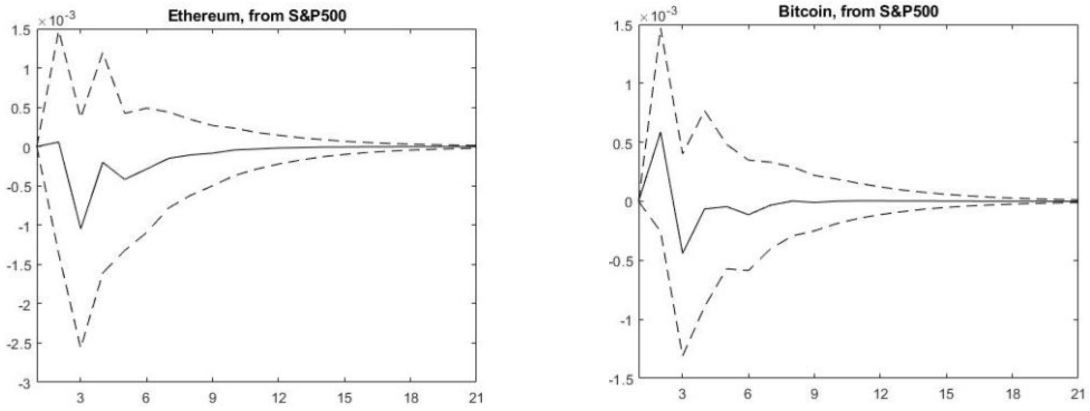

(a) Response of ETH (b) Response of BTC

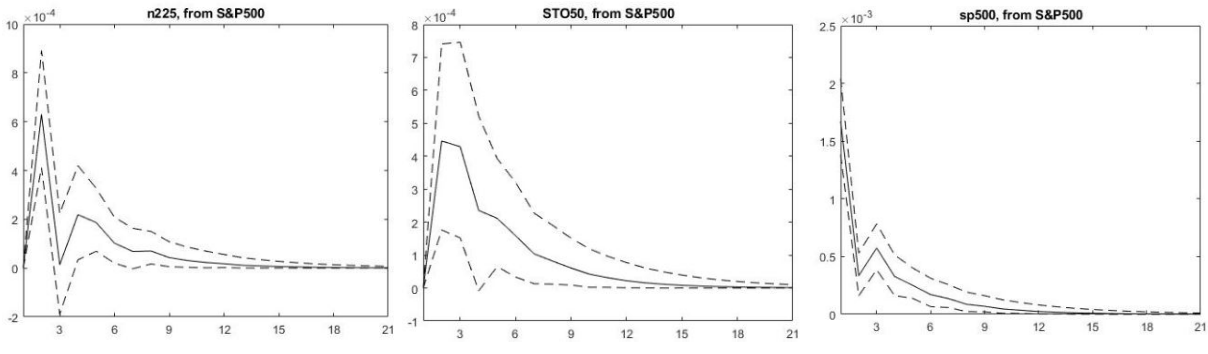

(c) Response of N225 (d) Response of STO50 (e) Response of SP500

Figure D.6: Orthogonalised impulse response functions, from an exogenous shock in S&P 500, with the 16th and 84th quantiles.

Appendix E

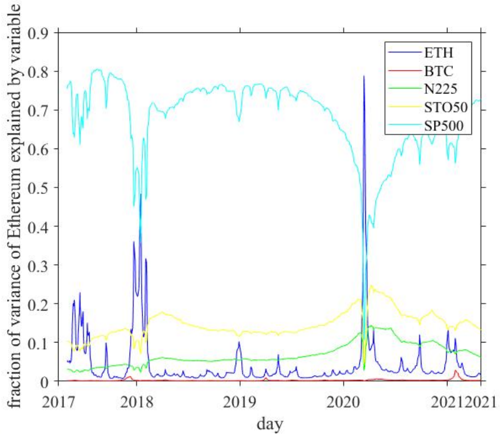

(a) FEVD of ETH, 10 day horizon

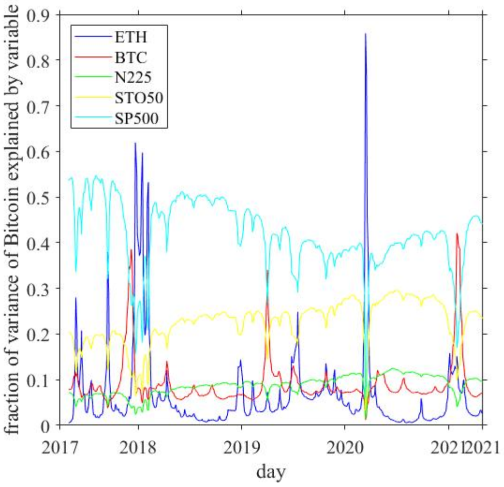

(b) FEVD of BTC, 10 day horizon

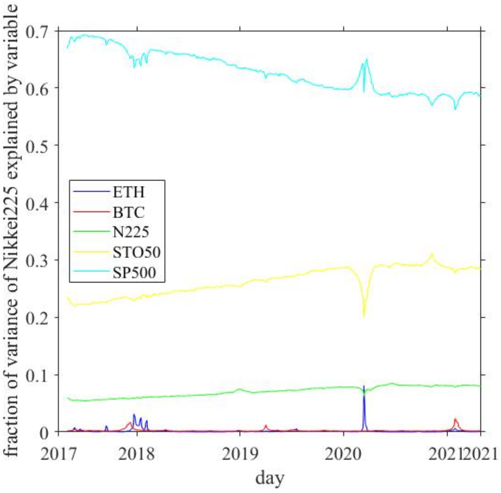

(c) FEVD of N225, 10 day horizon

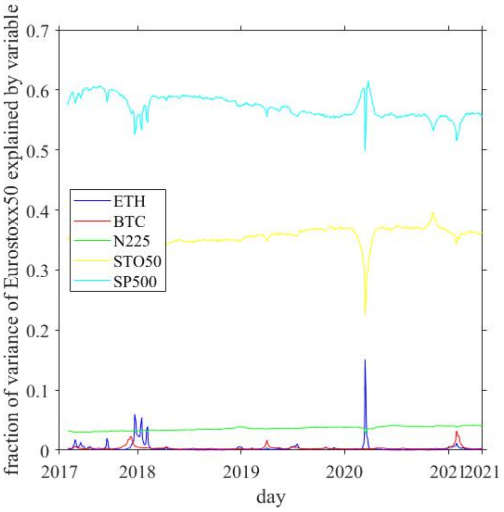

(d) FEVD of STO50, 10 day horizon

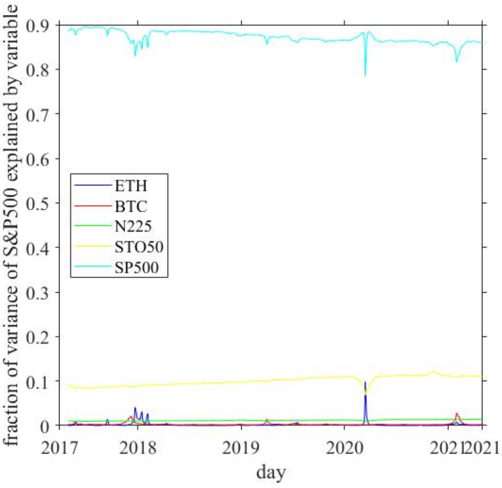

(e) FEVD of SP500, 10 day horizon

Figure E.1: Forecast error variance decomposition of all markets for 10 day horizon for RS_t^+.

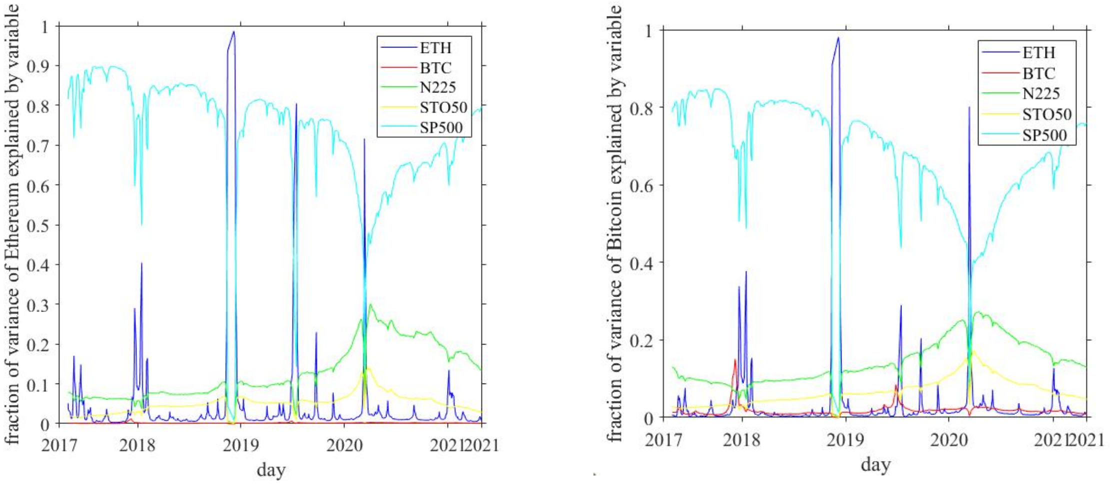

(a) FEVD of ETH, 10 day horizon

(b) FEVD of BTC, 10 day horizon

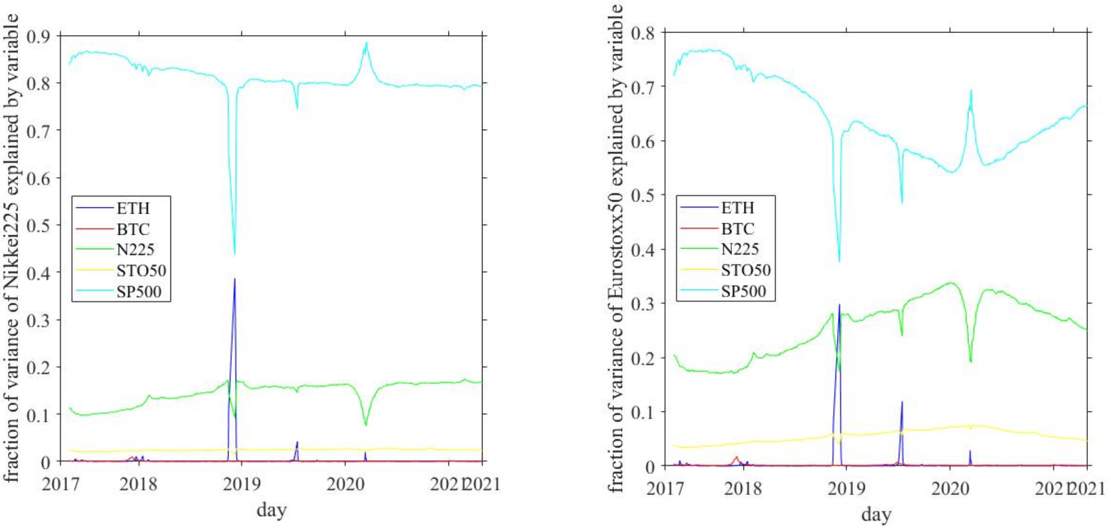

(c) FEVD of N225, 10 day horizon

(d) FEVD of STO50, 10 day horizon

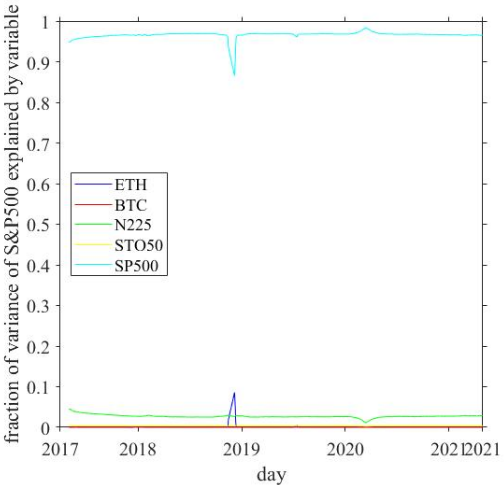

(e) FEVD of SP500, 10 day horizon

Figure E.2: Forecast error variance decomposition of all markets for 10 day horizon for RS_t^-.

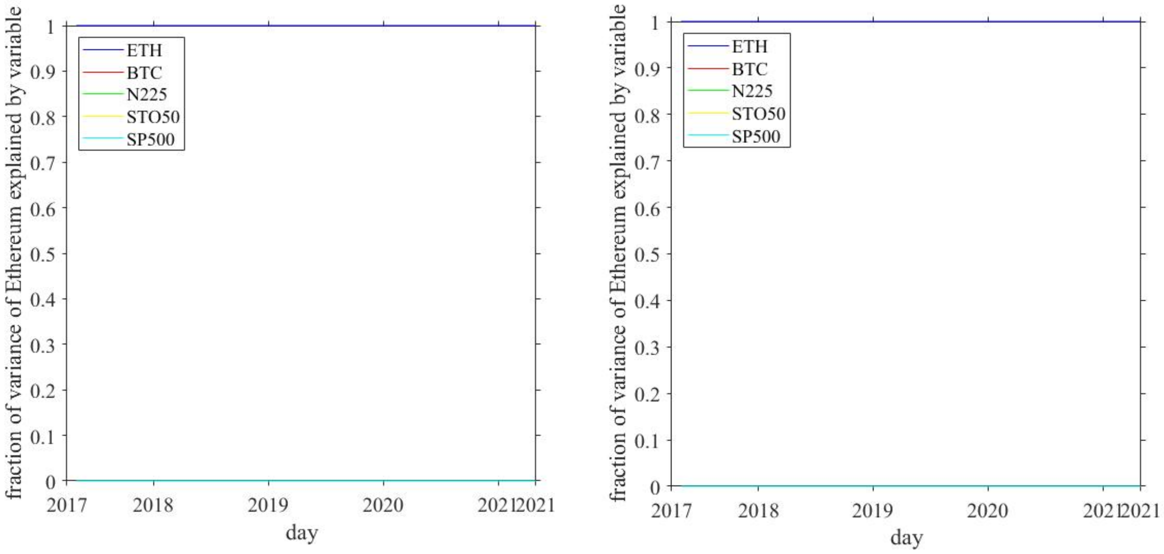

(a) FEVD of ETH for RS_t^+

(b) FEVD of ETH for RS_t^-

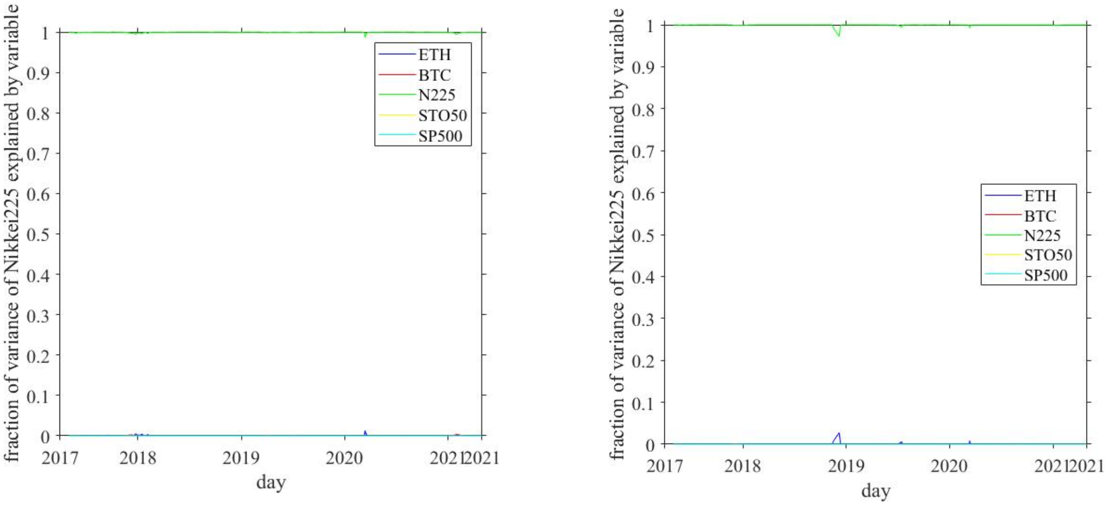

(c) FEVD of N225 for RS_t^+

(d) FEVD of N225 for RS_t^-

Figure E.3: Forecast error variance decompositions of ETH and N225 for 1 day horizon for RS_t^+ and RS_t^-.

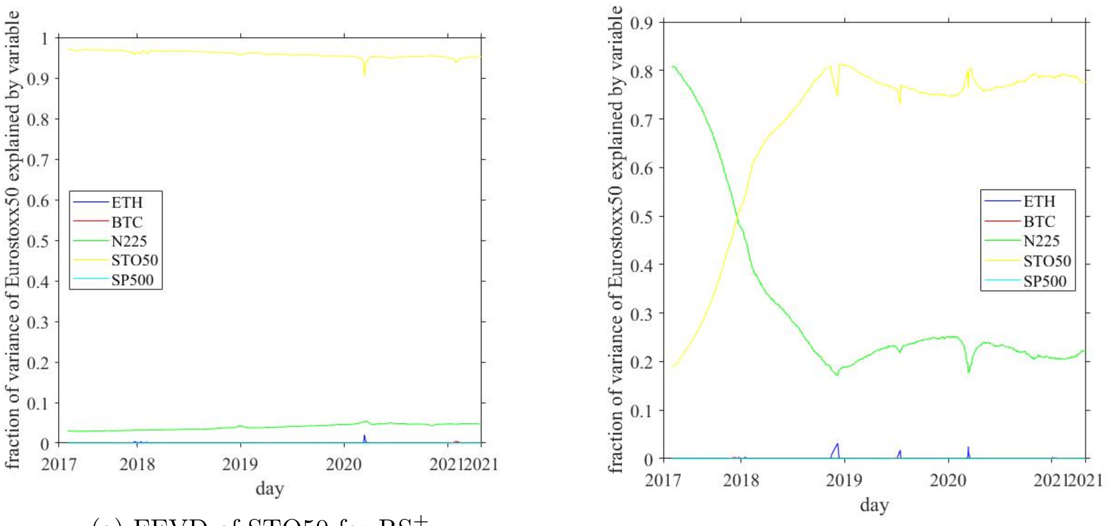

(a) FEVD of STO50 for RS_t^+

(b) FEVD of STO50 for RS_t^-

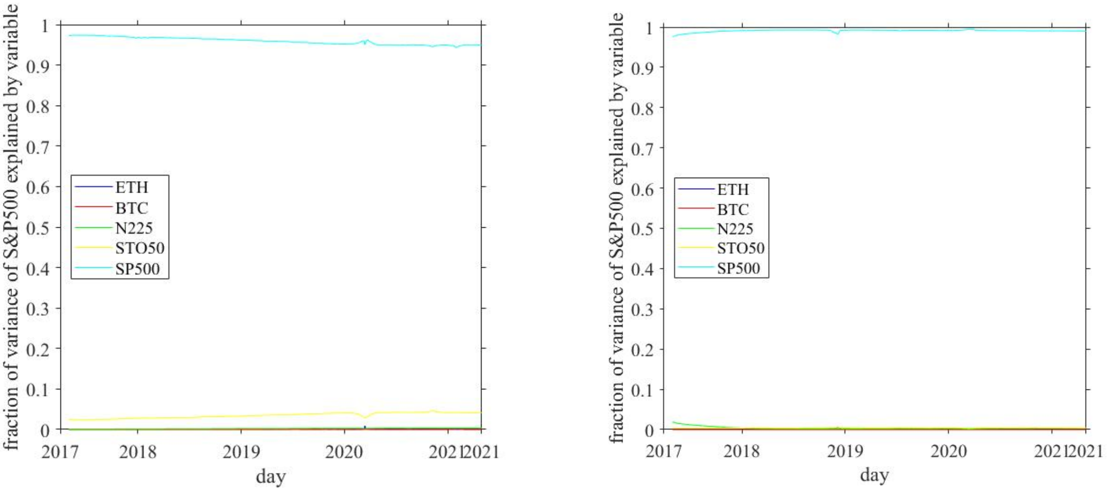

(c) FEVD of SP500 for RS_t^+

(d) FEVD of SP500 for RS_t^-

Figure E.4: Forecast error variance decompositions of STO50 and SP500 for 1 day horizon for RS_t^+ and RS_t^-.